JOURNAL OF GEOPHYSICAL RESEARCH: ATMOSPHERES, VOL. 118, 3066–3084, doi:10.1002/jgrd.50277, 2013

# A comparison of parameterizations of incoming longwave radiation over melting glaciers: Model robustness and seasonal variability

I. Juszak[1,2] and F. Pellicciotti[1]

Received 23 April 2012; revised 14 December 2012; accepted 14 February 2013; published 19 April 2013.

[1] Parameterizations of incoming longwave radiation are increasingly receiving attention for both low and high elevation glacierized sites. In this paper, we test 13 clear-sky parameterizations combined with seven cloud corrections for all-sky atmospheric emissivity at one location on Haut Glacier d'Arolla. We also analyze the four seasons separately and conduct a cross-validation to test the parameters' robustness. The best parameterization is the one by Dilley and O'Brien, B for clear-sky conditions combined with Unsworth and Monteith cloud correction. This model is also the most robust when tested in cross-validation. When validated at different sites in the southern Alps of Switzerland and north-western Italian Alps, all parameterizations show a substantial decrease in performance, except for one site, thus suggesting that it is important to recalibrate parameterizations of incoming longwave radiation for different locations. We argue that this is due to differences in the structure of the atmosphere at the sites. We also quantify the effect that the incoming longwave radiation parameterizations have on energy-balance melt modeling, and show that recalibration of model parameters is needed. Using parameters from other sites leads to a significant underestimation of melt and to an error that is larger than that associated with using different parameterizations. Once recalibrated, however, the parameters of most models seem to be stable over seasons and years at the location on Haut Glacier d'Arolla.

**Citation:** Juszak, I., and F. Pellicciotti (2013), A comparison of parameterizations of incoming longwave radiation over melting glaciers: Model robustness and seasonal variability, *J. Geophys. Res. Atmos.*, *118*, 3066–3084, doi:10.1002/jgrd.50277.

## 1. Introduction

[2] Incoming longwave radiation is an important source of energy for melt over glaciers, especially during cloudy periods and in high-latitude environments [*Sicart et al.*, 2006; *Mölg et al.*, 2009]. Its quantification, however, depends on the way the fluxes are regarded. If the incoming and outgoing longwave radiation fluxes are considered separately, incoming longwave radiation can be the highest source of energy for melt [*Ohmura*, 2001]. Most of the studies on energy fluxes over melting glaciers, however, consider the net longwave radiation flux, calculated as the difference between the incoming and outgoing flux, in which case the two almost cancel out each other. In addition, incoming longwave radiation is a relatively constant flux over the day, unlike the incoming shortwave radiation, which is high during the day and zero at night [e.g., *Pellicciotti et al*., 2008]. For this reason, a large part of the energy supplied by incoming longwave radiation is provided when no melt occurs and is therefore not used directly for melt. If we consider the mean flux over the hours when melt occurs, then the shortwave radiation flux will be higher on clear-sky days. Because of this importance, large attention has been given to the shortwave radiation flux in studies of energy balance and ablation over glaciers [e.g., *Munro and Young*, 1982; *Cutler and Munro*, 1996; *Arnold et al*., 1996; *Brock et al*., 2000a; *Anslow et al*., 2008; *Mölg et al*., 2009; *Pellicciotti et al*., 2011]. Only recently, workers have looked at comparative modeling of incoming longwave radiation over melting glaciers [e.g., *Sedlar and Hock*, 2009; *Sicart et al*., 2010].

[3] As suggested by *Dilley and O'Brien* [1998], parameterizations of incoming longwave radiation can be grouped into three main categories: (i) simple parameterizations that calculate longwave irradiance in terms of surface or screen level meteorological variables, (ii) models requiring some specification of the vertical structure of the atmosphere, and (iii) complete solutions of the radiative transfer equation [*Dilley and O'Brien*, 1998; *Niemelä et al.*, 2001]. All models tested in this work belong to the first category, while parameterizations which require coarse profiles of temperature and moisture [e.g., *Gupta*, 1989; *Gupta et al*., 1992; *Niemelä et al*., 2001] fall into the second category. The radiation models used in General Circulation Models (GCMs) are an example of the third category, as they

[1]Institute of Environmental Engineering, ETH Zurich, Zurich, Switzerland.
[2]Currently at Institute of Evolutionary Biology and Environmental Studies, University of Zurich, Zurich, Switzerland.

Corresponding author: I. Juszak, Institute of Evolutionary Biology and Environmental Studies, University of Zurich, Zurich, Switzerland. (inge.juszak@ieu.uzh.ch)


2169-897X/13/10.1002/jgrd.50277

allow computation of profiles of irradiance and atmospheric heating but require detailed vertical profiles of temperature, moisture, and clouds. For many glaciological applications, only models of the first category can be used due to the lack of more detailed data. Several studies have evaluated the performance of those models for low land locations [e.g., *Hatfield et al*., 1983; *Alados-Arboledas*, 1993; *Sugita and Brutsaert*, 1993; *Alados-Arboledas et al*., 1995; *Prata*, 1996; *Niemelä et al*., 2001; *Iziomon et al*., 2003; *Finch and Best*, 2004; *Flerchinger et al*., 2009; *Abramowitz et al*., 2012; *Marthews et al*., 2012]. Some of these studies compared simulations and observations at multiple locations [*Hatfield et al.*, 1983; *Prata*, 1996; *Flerchinger et al.*, 2009; *Abramowitz et al.*, 2012], while others have tested different parameterizations at one location or area [e.g., *Alados-Arboledas*, 1993; *Sugita and Brutsaert*, 1993; *Alados-Arboledas et al*., 1995; *Niemelä et al*., 2001; *Sedlar and Hock*, 2009; *Marthews et al*., 2012]. *Finch and Best* [2004] used a radiative transfer model as benchmark for several longwave radiation models. *Sugita and Brutsaert* [1993], *Niemelä et al.* [2001], *Iziomon et al.* [2003], and *Sedlar and Hock* [2009] focused on recalibration of model parameters, while *Hatfield et al.* [1983], *Alados-Arboledas* [1993], *Alados-Arboledas et al.* [1995], *Prata* [1996], *Finch and Best* [2004], and *Flerchinger et al.* [2009] tested various parameterizations with the original parameter values. *Flerchinger et al.* [2009] is the only study that tested a large range of clear-sky and all-sky incoming longwave radiation parameterizations at multiple sites. They applied 13 parameterizations with their original parameters for clear-sky conditions, 10 cloud corrections, and 4 all-sky parameterizations, but did not look at glacierized sites in particular.

[4] In this work, we intend to test the suitability of the parameterizations that have been suggested in the literature for both clear-sky and all-sky conditions, with specific attention to high mountain locations and melting surfaces. We also look at the model robustness by dividing the available data set in a calibration and validation subset and performing a cross-validation with variable number of years. Each parameterization is calibrated and validated for the four seasons separately, in order to identify the seasonal variability and quantify its importance. For this, we use a 7 year data set collected at a permanent Automatic Weather Station (AWS) installed near the terminus of Haut Glacier d'Arolla, Switzerland (Figure 1). We also test the parameterizations at four additional sites in the Swiss and Italian Alps to investigate their transferability in space. Finally, we test the impact of the various parameterizations on melt modeling by implementing the parameterizations in an energy balance model and quantifying the differences in melt total at one location on Haut Glacier d'Arolla.

[5] Our work provides one of the first analyses of both clear-sky and all-sky parameterizations for the Swiss Alps. We also examine the effects of seasonal variability in detail. We are not aware of other studies comparing different seasons in terms of applicability of incoming longwave radiation parameterizations, as most studies include all seasons in one data set [*Sugita and Brutsaert*, 1993; *Alados-Arboledas*, 1993; *Alados-Arboledas et al.*, 1995; *Prata*, 1996; *Iziomon et al.*, 2003; *Finch and Best*, 2004; *Flerchinger et al.*, 2009; *Sicart et al.*, 2010; *Abramowitz et al.*, 2012; *Gubler et al.*, 2012], or focus on one season only [*Hatfield et al.*, 1983; *Sugita and Brutsaert*, 1993; *Niemelä et al.*, 2001; *Sedlar and Hock*, 2009]. In comparison to the five works on a glacierized environment, our study presents a number of improvements. *Sedlar and Hock* [2009] analyzed one station on Storglaciären, Northern Sweden, and did not validate the model parameters at other locations. Their analysis of seven clear-sky and three all-sky parameterizations focused only on the summer season. *Sicart et al.* [2010] investigated the performance of only one parameterization on two tropical Andean glaciers. *MacDonell et al.* [2013] analyzed data from two Andean glaciers. To our knowledge, *Gubler et al.* [2012] is the only other study focusing on radiation modeling and model comparison in the Swiss Alps, but they include only two high alpine data sets and do not compare different cloud corrections. Finally, *Pellicciotti et al.* [2008] examined differences in the performance of two parameterizations on a glacier in the dry Andes of Chile for one season together with their impact on energy balance simulations.

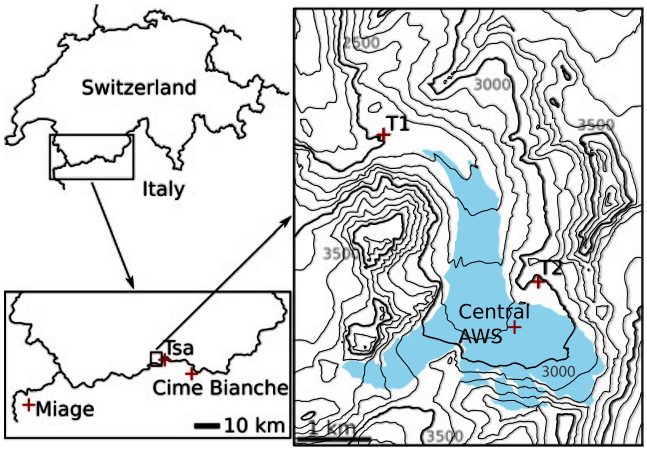


**Figure 1.** Location of the five study sites in Switzerland and Italy. The right plot shows Haut Glacier d'Arolla (in blue) with the position of the stations T1, T2, and the Central AWS. The latter is only used for testing the impact of different parameterizations on an energy balance melt model.

## 2. Data

[6] The ability of the parameterizations to reproduce measured incoming longwave radiation in an Alpine environment is tested at several AWSs in the Monte Rosa and Mont Blanc area. The data analysis and calibration are conducted at station T1 near the terminus of Haut Glacier d'Arolla (Figure 1). The calibrated parameterizations are then transferred to four other stations. T1 is chosen as the main station as it has the most extensive data set and the smallest number of missing values.

[7] The station T2 lies about 3 km south-east of T1, above Haut Glacier d'Arolla. Like T1, the station is not located on the glacier but close to it. The second validation station is located on Haut Glacier de Tsa de Tsan, which lies directly east of Haut Glacier d'Arolla, only separated from it through the Col du M. Brulé. The highest part of Haut Glacier de Tsa de Tsan has an elevation of about 3800 m above sea level (asl), while the elevation of the AWS

**Table 1.** Characteristics of the Locations of the Automatic Weather Stations (AWSs) Used in This Work[a]

| Name | Location | Elevation | Latitude | Longitude | Environment | $\alpha$ | Measurement Period |
|---|---|---|---|---|---|---|---|
| T1 | Haut Glacier d'Arolla | 2500 m | 45°59′25″ | 7°30′23″ | periglacial, rock | 20.4° | 28/11/2000–31/12/2007 |
| T2 | Haut Glacier d'Arolla | 2990 m | 45°58′20″ | 7°32′01″ | periglacial, debris | 19.5° | 26/11/2005–28/06/2007 |
| Miage[b,d] | Miage Glacier | 2030 m | 45°46′57″ | 6°52′37″ | glacial, debris | 18.2° | 12/06/2005–08/09/2005<br>05/06/2006–05/09/2006<br>20/06/2007–05/09/2007 |
| Tsa[c] | Haut Glacier de Tsa de Tsan | 3250 m | 45°59′ | 7°33′49″ | glacial, ice | 11.7° | 24/05/2007–15/10/2007 |
| Cime Bianche[c,d] | Breuil Cervinia | 3100 m | 45°55′ | 7°41′ | periglacial, rock | 6.3° | 14/03/2006–25/01/2010 |
| Central AWS | Haut Glacier d'Arolla | 2920 m | 45°58′00″ | 7°31′46″ | glacial, ice | | 23/07/2001–12/09/2001 |

[a] $\alpha$ is the mean elevation angle of the surrounding terrain. Dates are formatted as day/month/year.
[b] Data supplied by Ben Brock, University of Dundee.
[c] Data supplied by Edoardo Cremonese, Agenzia Regionale per la Protezione dell'Ambiente Valle d'Aosta.
[d] Elevation data taken from ASTER GDEM which is a product of METI and NASA.

is 3250 m. The distance to T1 is about 4.2 km. The station Cime Bianche is located nearby a glacier at about 3100 m asl. The location is about 15.7 km south east of T1. The AWS on the Miage glacier is the furthest from T1 (about 54 km) in the Mont Blanc area. The basic information on the stations can be found in Table 1, while their locations are shown in Figure 1.

[8] At T1, the four radiative fluxes are measured with a CNR1 (Kipp and Zonen) Net Radiometer. The measurement error given by the manufacturer is ±10% (daily value) which is about ±15 W m$^{-2}$ for incoming shortwave radiation and ±25 W m$^{-2}$ for longwave radiation [*Campbell*, 2009]. This limits the possible accuracy of the parameterizations. The characteristics of all the sensors from the calibration and validation stations are summarized in Table 2. The instruments used for the measurements at Haut Glacier d'Arolla Central AWS are described in more detail in *Pellicciotti et al.* [2008] and *Strasser et al.* [2004], while the Miage station and data set are described in *Brock et al.* [2010] and the station on Tsa de Tsan in *Cremonese et al.* [2007].

[9] The quality of data collected at high elevation, glacierized sites with sensors that are not inspected regularly might be affected by the presence of ice, snow, or frost on the sensor [e.g., *Halldin and Lindroth*, 1992; *Marty et al*., 2002; *MacDonell et al*., 2013]. This is very difficult to quantify in the absence of a setup specifically designed. However, two studies from several locations in Antarctica [*van den Broeke et al.*, 2004; *van As et al.*, 2005] have shown that even unventilated CNR1 sensors had a daily total accuracy better than 10% (given by the manufacturer, Table 2). It should be noticed, however, that in Antarctica, the low water content of the atmosphere is likely to make problems of rimming on the sensors less frequent than in the European Alps. *Marty et al.* [2002] used ventilated and shielded instruments at three high elevation sites in the Swiss Alps, together with modified Eppley pyrgeometers. These employ three dome thermistors instead of one only to provide a more representative dome temperature than in the standard CNR1. With these improvements, *Marty et al.* [2002] obtained a reduction in the uncertainty of 2 min averaged longwave radiation from 15 to about 3 W m$^{-2}$, which is much better than the values that can be obtained with standard measurements. Given that we used only the standard CNR1 setup, we refer to the study by *Michel et al.* [2008] for an estimate of the real uncertainty of the measurements. *Michel et al.* [2008] compared CNR1 with and without heating and ventilation to high standards reference instruments with very high accuracy (of about 1% for daily totals). Heating and ventilation are meant to prevent dew and ice formation on the glass dome. They obtained for the non-ventilated sensor a root mean square error of hourly averaged longwave radiation of 15.6 W m$^{-2}$ in comparison to the reference sensor. We assume that this can be regarded

**Table 2.** Characteristics of the Sensors Installed at the Automatic Weather Stations (AWSs) Used in This Work

| Measured Variable | Manufacturer | Sensor | Accuracy | Range | Location |
|---|---|---|---|---|---|
| Shortwave radiation | Kipp and Zonen | CM7B | ±5% | 305 to 2800 nm | Central AWS |
| | Kipp and Zonen | CM3 (CNR1) | ±10% | 305 to 2800 nm | T1, T2, Tsa, Miage |
| | Kipp and Zonen | CNR4 | ±10% | 305 to 2800 nm | Cime Bianche |
| Longwave radiation | Kipp and Zonen | CG3 (CNR1) | ±10% | 5000 to 50,000 nm | T1, T2, Tsa, Miage |
| | Kipp and Zonen | CNR4 | ±10% | 4500 to 42000 nm | Cime Bianche |
| Relative humidity | Rotronic | MP-103A | ±1% | 0 to 100% | T1, T2, Central AWS |
| | Vaisala | QMH101 | ±1% | 0 to 100% | Tsa |
| | Vaisala | HMP45C | ±2% (0 to 90%),<br>±3% (90 to 100%) | 0 to 100% | Miage |
| | Vaisala | HMP45A | ±2% (0 to 90%),<br>±3% (90 to 100%) | 0 to 100% | Cime Bianche |
| Air temperature | Rotronic | MP-103A | ±0.3°C | –40 to +60°C | T1, T2, Central AWS |
| | Vaisala | QMH101 | ±0.3°C | –40 to +60°C | Tsa |
| | Vaisala | HMP45C | ±0.2°C | –40 to +60°C | Miage |
| | Vaisala | HMP45A | ±0.2°C | –39.2 to +60°C | Cime Bianche |

**Table 3.** Basic Statistics for Measured Incoming Longwave Radiation at Station T1[a]

| | Spring | Summer | Autumn | Winter | Year |
|---|---|---|---|---|---|
| | | *Mean (W m$^{-2}$)* | | | |
| All | 255.6 | 298.7 | 272.1 | 234.2 | 263.8 |
| Clear-sky | 217.1 | 273.2 | 243.5 | 199.3 | 233.6 |
| Partly cloudy | 280.5 | 315.3 | 283.8 | | |
| Overcast | 269.8 | 330.9 | 308.4 | | |
| Day | 263.6 | 304.6 | 277.1 | 233.0 | 274.7 |
| Night | 249.9 | 292.9 | 269.4 | 234.4 | 257.4 |
| | | *Standard Deviation (W m$^{-2}$)* | | | |
| All | 43.9 | 31.4 | 37.9 | 42.8 | 46.3 |
| Clear-sky | 29.8 | 22.3 | 24.1 | 20.7 | 37.6 |
| Partly cloudy | 36.0 | 24.7 | 39.7 | | |
| Overcast | 46.3 | 13.8 | 28.7 | | |
| Day | 43.0 | 28.5 | 36.3 | 43.4 | 45.1 |
| Night | 43.9 | 33.0 | 38.4 | 42.7 | 45.9 |

[a]Clear-sky conditions are defined based on the measured incoming longwave radiation (see section 3.1 for details). Partly cloudy hours have a cloud cover between 0.4 and 0.6, and overcast conditions above 0.8. Night and day are distinguished by a threshold of 70 W m$^{-2}$ in the calculated potential incoming shortwave radiation. In winter at T1, no cloud-cover estimate is possible due to shading of the station (section 3.1).

as the minimum uncertainty of our measurements, given that at our high elevation sites, the occurrence of frost and dew might be more frequent than at the Payerne site (at 490 m asl) used for the study of *Michel et al.* [2008].

[10] The data are corrected for implausible values and aggregated to hourly values. All hourly values were within expected ranges. At T1, the period between autumn 2001 and summer 2002 is discarded as the humidity and temperature sensors did not work correctly.

[11] The analysis in this paper is conducted at the hourly time scale for all four seasons separately. The first reason is the need of a parameterization optimized for the melt season to improve energy balance modeling on the glacier. In this work, the main melt season is defined as the summer months June, July, and August. The second reason is the topography at T1. The station is completely shaded between 8 November and 7 February, thus preventing the estimation of cloud cover from incoming solar radiation. Therefore, this period is taken as winter at T1. For the validation at other stations, the winter is defined as December, January, and February.

[12] The basic statistics of the incoming longwave radiation record at T1 are shown in Table 3. In general, overcast days exhibit higher incoming longwave radiation than clear-sky days, because water droplets and vapor in clouds emit more radiation than the clear-sky atmosphere [e.g., *Brunt*, 1932; *Sicart et al*., 2006]. Variability of incoming longwave radiation is larger on partly cloudy and overcast days because these categories include a variety of cases. The cloud-cover value (as calculated using the model described in section 3.1) does not include information on height and temperature of the clouds, which influence the incoming longwave radiation significantly. The difference between night and day is relatively small but consistent with the temperature maximum. The different seasons show considerable variations. The mean value of incoming longwave radiation is correlated to the temperature. Thus, it is highest in summer, followed by autumn, spring, and winter. The highest standard deviations occur in spring and winter, while the summer values are least variable.

[13] Analysis of the records at the four validation sites indicates differences between the longwave radiation records at the AWSs in mean behavior and variability. A systematic comparison of the data sets is not possible as they cover a different period over the year and are averaged over a different number of years. However, to understand more about the variation between the data sets, an overview of the data is presented in Figure 2. It shows the mean monthly pattern over the period of record for all five locations. The incoming longwave radiation is higher at T1 and Miage, while the smallest average monthly values can be found at Cime Bianche. Not only the mean monthly values

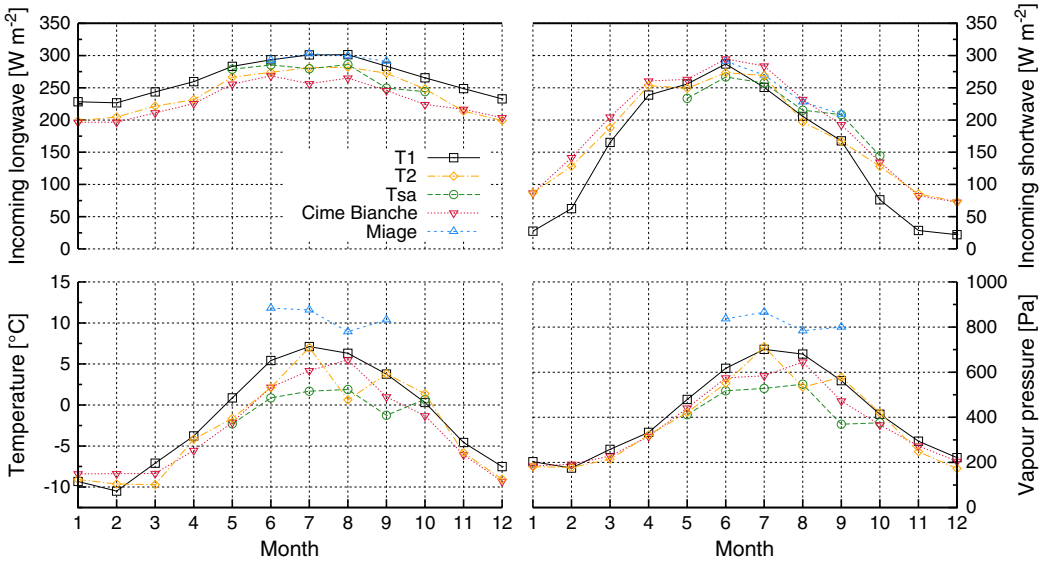


**Figure 2.** Seasonal variations of air temperature, vapor pressure, and incoming longwave and shortwave radiation at all five stations averaged over the entire period of record (see Table 1).

**Table 4.** Parameterizations of Clear-Sky Emissivity $\varepsilon_{cs}$ Used in This Work[a]

| Parameterization | | | Original Parameters | Data |
|---|---|---|---|---|
| 1 | *Ångström* [1916] | $\varepsilon_{cs} = a - b \cdot \exp[-c \cdot e_a]$ | $a = 0.73$<br>$b = 0.26$<br>$c = 0.00052$ | Algeria, California, 20°; (d) |
| 2 | *Brunt* [1932] | $\varepsilon_{cs} = a + b \cdot \sqrt{e_a}$ | $a = 0.47$<br>$b = 0.0072$ | Algeria, Europe; (d / m), nocturnal |
| 3 | *Swinbank* [1963] | $\varepsilon_{cs} = \frac{10^{a+1}}{\sigma} \cdot T_a^{b-4}$ | $a = -13.638$<br>$b = 6.148$ | Great Britain; (m) |
| 4 | *Idso and Jackson* [1969] | $\varepsilon_{cs} = 1 - a \cdot \exp\left[-b \cdot (273 - T_a)^2\right]$ | $a = 0.261$<br>$b = 0.00077$ | Alaska Arizona, Australia, Indian Ocean |
| 5 | *Maykut and Church* [1973] | $\varepsilon_{cs} = a$ | $a = 0.7855$ | Alaska; (m) |
| 6 | *Satterlund* [1979] | $\varepsilon_{cs} = a \cdot \left(1 - \exp\left[-(e_a/100)^{(T_a/b)}\right]\right)$ | $a = 1.08$<br>$b = 2016$ | Alaska, Montana; (d) |
| 7 | *Idso* [1981] | $\varepsilon_{cs} = a + b \cdot e_a \cdot \exp[c/T_a]$ | $a = 0.7$<br>$b = 5.95 \cdot 10^{-7}$<br>$c = 1500$ | Arizona |
| 8 | *Konzelmann et al.* [1994] | $\varepsilon_{cs} = a + b \cdot \left(\frac{e_a}{T_a}\right)^c$ | $a = 0.23$<br>$b = 0.484$<br>$c = 1.8$ | Greenland; (h) |
| 9 | *Prata* [1996] | $\varepsilon_{cs} = 1 - (1 + w) \cdot \exp\left[-(a + b \cdot w)^c\right]$ | $a = 1.2$<br>$b = 3$<br>$c = 0.5$ | various |
| 10 | *Dilley and O'Brien* [1998], A | $\varepsilon_{cs} = 1 - \exp\left[-1.66 \cdot \left(a + b \cdot \frac{T_a}{273.16} + c \cdot \sqrt{\frac{w}{25}}\right)\right]$ | $a = 2.232$<br>$b = -1.875$<br>$c = 0.7356$ | satellite (TOVS)<br>TIGR data of all latitudes |
| 11 | *Dilley and O'Brien* [1998], B | $\varepsilon_{cs} = \frac{a + b \cdot \left(\frac{T_a}{273.16}\right)^6 + c \cdot \sqrt{\frac{w}{25}}}{\sigma \cdot T_a^4}$ | $a = 59.38$<br>$b = 113.7$<br>$c = 96.96$ | satellite (TOVS)<br>TIGR data of all latitudes |
| 12 | *Niemelä et al.* [2001] | $\varepsilon_{cs} = a + b \cdot (e_a - c)$ | $a = 0.72$<br>$b = 0.00009$ for $e_a \geq 200$<br>$b = -0.00076$ for $e_a < 200$<br>$c = 200$ | Finland; (h), nocturnal |
| 13 | *Iziomon et al.* [2003] | $\varepsilon_{cs} = 1 - a \cdot \exp[-b \cdot e_a/T_a]$ | $a = 6.2647 \cdot 10^{-5}h + 0.33672$<br>$b = 1.1746 \cdot 10^{-5}h + 0.09751$ | Germany; (h) |

[a] $e_a$ is vapor pressure at screen level (in Pa), $T_a$ is air temperature at screen level (in K), $h$ is the elevation of the station (in m), and $w$ is precipitable water (in kg m$^{-2}$). The data column indicates the origin of the data used for the derivation of the formula as well as the temporal resolution (hourly (h), daily (d), or monthly (m)) of the data for which the parameterization was developed. Where no indication is provided, the temporal resolution was not indicated in the original paper. All parameterizations will be referred to with the first author's name, except for the two parameterizations of Idso, which will be referred to as Idso69 and Idso81 (indexes 4 and 7, respectively) and the two parameterizations of *Dilley and O'Brien* [1998], which will be referred to as Dilley A and Dilley B.

of incoming longwave radiation differ between the stations but also the variability. While the standard deviation of the measured downwelling longwave radiation data at T1 is 46 W m$^{-2}$, it is 57 W m$^{-2}$ at T2, 38 W m$^{-2}$ at Tsa de Tsan, 59 W m$^{-2}$ at Cime Bianche, and 45 W m$^{-2}$ at Miage. It has to be noted that the data at Tsa de Tsan and Miage only include summer values while the other stations measure during the whole year. Compared to T2 and Cime Bianche, the incoming longwave radiation at T1 seems to be less variable, also when the common period is considered (Figure 8 in section 5). In winter, the incoming shortwave radiation is lower at T1 than at the other AWS as the station is shaded. Shading decreases the mean air temperature and thus the longwave radiation from the surrounding atmosphere at T1. The mean air temperature is also influenced by the elevation of the stations. On average, the air is warmer at the Miage AWS (the lowest site) followed by T1, while the coldest temperatures are evident at the station on Tsa de Tsan, which is the highest of our sites. However, additional local effects influence the air temperature. At Miage, temperatures are affected by the debris covering the surface, which causes high emission of longwave radiation from the surface and a corresponding warming of the air above the surface [*Brock et al.*, 2010]. T1, which is located below Haut Glacier d'Arolla, is affected by cold glacier winds [*Dadic et al.*, 2008]. Contrary to T1, T2 is located above the glacier in a topographic bowl which warms up more than other sites at the same elevation [*Dadic et al.*, 2008]. A similar variation as for the temperature is evident for the vapor pressure, which is closely linked with temperature.

**Table 5.** Parameterizations of Emissivity for Cloudy Conditions $\varepsilon_a$[a]

| Parameterization | | | Original parameters | Data |
|---|---|---|---|---|
| 1 | *Bolz* [1949] | $\varepsilon_a = \varepsilon_{cs} \cdot \left(1 + a \cdot n^b\right)$ | $a = 0.22$<br>$b = 2.5$ | Germany; (h) |
| 2 | *Marshunova* [1961]<br>(from *König-Langlo and Augstein* [1994]) | $\varepsilon_a = (1 + a \cdot n) \cdot \left(b + c\sqrt{e_a/100}\right)$ | $a = 0.275$<br>$b = 0.67$<br>$c = 0.05$ | |
| 3 | *Unsworth and Monteith* [1975] | $\varepsilon_a = \varepsilon_{cs} \cdot (1 + a \cdot n) + b \cdot n$ | $a = -0.84$<br>$b = 0.84$ | Great Britain; Sudan; (m) |
| 4 | *Kimball et al.* [1982] | $\varepsilon_a = \varepsilon_{cs} + \tau_8 n f_8$<br>$\tau_8 = 1 - \varepsilon_{8z} \cdot (a - b\varepsilon_{8z})$<br>$\varepsilon_{8z} = 0.24 + 2.98 \cdot 10^{-6} \left(\frac{e_a}{1000}\right)^2 \exp[3000/T_a]$<br>$f_8 = -0.6732 + 6.24 \cdot 10^{-3} T_a - 9.14 \cdot 10^{-6} T_a^2$ | $a = 1.4$<br>$b = 0.4$ | USA; (h) |
| 5 | *König-Langlo and Augstein* [1994] | $\varepsilon_a = a + b \cdot n^c$ | $a = 0.765$<br>$b = 0.22$<br>$c = 3$ | Arctic, Antarctic |
| 6 | *Konzelmann et al.* [1994] | $\varepsilon_a = \varepsilon_{cs} \cdot (1 - n^a) + b \cdot n^a$ | $a = 4$<br>$b = 0.952$ | Greenland; (h) |
| 7 | *Crawford and Duchon* [1999] | $\varepsilon_a = \varepsilon_{cs} \cdot (1 - n) + n$ | | Oklahoma; (0.5 h) |
| 8 | *Lhomme et al.* [2007] | $\varepsilon_a = \varepsilon_{cs} \cdot (a + b \cdot n)$ | $a = 1.07$<br>$b = 0.34$ | Andean Altiplano; (h) |

[a] $n$ is cloud-cover, $\varepsilon_{cs}$ is clear-sky emissivity, $e_a$ is vapor pressure at screen level (in Pa), and $T_a$ is air temperature at screen level (in K). The data column indicates the origin of the data used for derivation of the formula as well as the temporal resolution of the data used for its derivation (half hourly (0.5 h), hourly (h), or monthly (m)). Where no indication is provided, the temporal resolution was not indicated in the original paper. All parameterizations will be referred to with the first author's name.

## 3. Methods

[14] Incoming longwave radiation is modeled using the Stefan-Boltzmann equation for a grey body

$$L\downarrow = \varepsilon_{\text{eff}}\, \sigma\, T_{\text{eff}}^4 \tag{1}$$

where $T_{\text{eff}}$ is effective temperature (K), $\sigma$ is the Stefan-Boltzmann constant ($5.67 \cdot 10^{-8}$ W m$^{-2}$ K$^{-4}$), and $\varepsilon_{\text{eff}}$ is the effective emissivity of the sky. By effective temperature, we refer to the average temperature representative of the part of the atmosphere that emits longwave radiation. The introduction of an effective temperature is necessary as the emitting atmospheric layer might not be isothermal.

[15] However, neither the effective temperature of the emitting atmospheric layer nor its emissivity is known. Following common practice [e.g., *Prata*, 1996; *Flerchinger et al*., 2009], the screen air temperature is used as representative of the lower atmosphere [*Ohmura*, 2001; *Gröbner et al.*, 2009]. The emissivity of clear skies ($\varepsilon_{cs}$) is estimated from 13 different empirical parameterizations which include the air temperature and/or vapor pressure (Table 4). For cloudy conditions, eight cloud corrections are used based on a cloud-cover estimate (Table 5). The cloud corrections provide an estimate of the all-sky emissivity ($\varepsilon_a$), which is the modeled apparent emissivity when the air temperature is used instead of the effective temperature.

### 3.1. Clear-Sky Conditions and Cloud-Cover

[16] As the clear-sky parameterizations can only be fitted on hours without clouds, a distinction between cloudy and clear-sky conditions is necessary. We adopt the approach by *Marty and Philipona* [2000], which has been extensively used in the literature [e.g., *Ruckstuhl and Philipona*, 2008; *Schade et al*., 2009; *Kuipers Munneke et al*., 2011; *Gubler et al*., 2012]. The method is based on measurements of incoming longwave radiation and thus is independent from daylight and topographical shading. The actual atmospheric emissivity is calculated from the measured incoming longwave radiation and the air temperature $T_a$ [K] with the Stefan-Boltzmann equation. It is then compared to the modeled emissivity the sky would have at clear sky conditions, which is estimated from $\varepsilon_c = \varepsilon_{ad} + k \cdot (e_a/T_a)^{1/8}$ where $e_a$ [Pa] is the vapor pressure. The parameters $\varepsilon_{ad}$ and $k$ are obtained from fitting the function on selected clear-sky data. Hours with an actual atmospheric emissivity less or equal to the modeled clear-sky emissivity are considered as clear-sky, the remaining data are not used for the derivation of the clear-sky parameters.

[17] The cloud correction formulae need cloud cover as an input variable, which is difficult to measure and not commonly observed. Some of the original cloud correction formulae use observations for the derivation [*Bolz*, 1949; *Unsworth and Monteith*, 1975; *Kimball et al.*, 1982; *König-Langlo and Augstein*, 1994; *Konzelmann et al.*, 1994], but observations are not available for this study, as for many others, such as *Sedlar and Hock* [2009], *Sicart et al.* [2010], *Gubler et al.* [2012], and *MacDonell et al.* [2013]. Various parameterizations have been developed to estimate cloud cover from the measured incoming solar radiation and the potential solar radiation for clear-sky conditions [e.g., *Laevastu*, 1960; *Kasten and Czeplak*, 1980; *Konzelmann et al*., 1994; *Greuell et al*., 1997; *Crawford and Duchon*, 1999; *Sedlar and Hock*, 2009].

[18] We compute potential incoming shortwave radiation using a nonparametric model described in *Pellicciotti et al.* [2011]. The model is based on *Iqbal* [1983] for the calculation of solar radiation transmission through the atmosphere and takes into account the interaction between the solar

radiation beam and topography, including multiple reflection between the surface and the atmosphere using the vectorial algebra approach proposed by *Corripio* [2003].

[19] We calculate cloud cover $n$ from the ratio of measured to potential incoming shortwave radiation as $n = 1 - \frac{S\downarrow_{\text{measured}}}{S\downarrow_{\text{pot}}}$ on an hourly scale following *Crawford and Duchon* [1999] and *Lhomme et al.* [2007]. We also tested equations proposed by other authors [*Laevastu*, 1960; *Kasten and Czeplak*, 1980; *Konzelmann et al.*, 1994; *Greuell et al.*, 1997; *Sedlar and Hock*, 2009], but they all resulted in smaller correlation coefficients between the estimated cloud cover and the measured longwave radiation. Thus, the analysis is restricted to one parameterization. At night, we use a linear interpolation between the mean cloud cover of the last 3 h of the day before and the mean of the first three morning hours of the following day. To distinguish between day and night, a threshold of 70 W m$^{-2}$ in the modeled potential clear-sky radiation is used.

[20] Unlike the other four stations, T1 is shaded during the whole day in winter. Thus, only diffuse shortwave radiation reaches the ground. Diffuse radiation is usually greater when the sky is (partly) cloud covered than on clear-sky days [*Kasten and Czeplak*, 1980]. In this season, therefore, no cloud-cover estimate is possible. Furthermore, a correction is needed from 28 September to 7 November and from 8 February to 16 March as in this time T1 is shaded at noon. In these periods, even small shifts in the records of radiation cause errors in the cloud cover because of the strong gradients in the clear-sky radiation. To overcome these limitations, a two-criteria model was applied to estimate the cloud cover at T1 in these periods. First, we tested if the measured shortwave radiation of a given day shows peak values at the same time as the potential radiation. Second, the ratio between the measured and the potential shortwave radiation at the time of the 2 h with the maximum values is computed. If the highest two measured values are each at least 70% of the highest two potential values of that day, the cloud cover of the day is set to zero. The low threshold of 70% is needed due to the uncertainty of the modeling of potential incoming shortwave radiation in this period. If the measured peaks are shifted significantly compared to the peaks in the potential shortwave radiation or the instrument receives less than 70% of the potentially available energy at the peak hours, the cloud cover of the whole day is calculated from the ratio of the measured to potential incoming shortwave radiation at the time of the highest peak in the potential radiation.

[21] The calculated cloud cover cannot be interpreted as the fraction of the sky which is obscured by clouds. It rather describes an integrated measure of cloud amount as well as cloud type, height, and optical depth.

### 3.2. Clear-Sky Parameterizations

[22] An overview of the 13 clear-sky parameterizations taken from the literature and tested on the data is shown in Table 4. The parameterizations by *Prata* [1996] and *Dilley and O'Brien* [1998] need precipitable water $w$ [kg m$^{-2}$] as input parameter. As this is not commonly measured, it is estimated using the approach suggested by *Prata* [1996]:

$$w = 4.65 \cdot \frac{e_a}{T_a} \tag{2}$$

where $e_a$ is the water vapor pressure (in Pa) and $T_a$ is the air temperature at screen level (in K).

[23] The classical approach by *Brutsaert* [1975] is not implemented, as it matches the parameterization by *Konzelmann et al*. [1994] with the parameter $a = 0$. The empirical formulae are adjusted to SI units, which implies a conversion of the original parameters for comparability.

### 3.3. All-Sky Parameterizations

[24] The emissivity of the atmosphere on cloudy days is commonly estimated from the clear-sky emissivity corrected with a term representing cloud cover. Some all-sky parameterizations also include water vapor pressure and air temperature. Although some of the algorithms were initially developed together with a specific clear-sky algorithm, we test all combinations of clear-sky parameterizations with all the cloud corrections. The parameterizations are listed in Table 5.

### 3.4. Calibration, Validation, and Transferability

[25] The evaluation of the model performance is based on the root mean square error (RMSE), the mean bias error (MBE), and the comparison of the observed and predicted standard deviations ($\sigma_o$ and $\sigma_p$). The three measures are defined as follows:

$$\text{RMSE} = \sqrt{\frac{1}{N}\sum_{i=1}^{N}(P_i - O_i)^2} \tag{3}$$

$$\text{MBE} = \frac{1}{N}\sum_{i=1}^{N}(P_i - O_i) \tag{4}$$

$$\sigma_o = \sqrt{\frac{1}{N-1}\sum_{i=1}^{N}\left(O_i - \overline{O}\right)^2} \tag{5}$$

$$\sigma_p = \sqrt{\frac{1}{N-1}\sum_{i=1}^{N}\left(P_i - \overline{P}\right)^2} \tag{6}$$

where $N$ is the number of measurements, and $O$ and $P$ are the observed and predicted values with arithmetic means $\overline{O}$ and $\overline{P}$, respectively. The error measures RMSE and MBE have been used in several modeling studies, among others by *Finch and Best* [2004] and *Sedlar and Hock* [2009].

[26] In a first step, the clear-sky parameterizations are calibrated and evaluated on all clear-sky hours of all individual seasons at T1. In a second step, the parameterizations are fitted to data of one, two, three, four, or five of the six available seasons in all possible combinations. The RMSE is then computed for the incoming longwave radiation of the seasons which are not used for calibration. With this cross-validation, the transferability in time and the robustness of the parameters are evaluated.

[27] All eight cloud corrections are then combined with each of the 13 calibrated clear-sky parameterizations. Winter is not considered at T1 due to the lack of cloud-cover information (see section 3.1). As for the clear-sky parameterizations, the cloud corrections are fitted to all data of each season in a first step. In a second step, the results are cross-validated using the division of the data set as described above.

**Table 6.** Root Mean Square Errors, RMSE, (W m$^{-2}$) of Modeled and Observed Data for All Clear-Sky Parameterizations for Clear-Sky Hours of the Entire Period (2000–2007) at T1[a]

| Season | Clear-Sky Parameterization | | | | | | | | | | | | |
|---|---|---|---|---|---|---|---|---|---|---|---|---|---|
| | 1 | 2 | 3 | 4 | 5 | 6 | 7 | 8 | 9 | 10 | 11 | 12 | 13 |
| Spring | 5.4 | 5.4 | 7.9 | 10.0 | 11.2 | 5.4 | 5.7 | 5.3 | 5.4 | **5.2** | **5.3** | 5.4 | 5.6 |
| Summer | 6.5 | 6.5 | 8.5 | 8.8 | 9.1 | 6.5 | 6.5 | 6.6 | 6.6 | **6.5** | **6.5** | 6.5 | 6.6 |
| Autumn | 6.4 | 6.5 | 9.5 | 10.6 | 10.6 | 6.4 | 6.6 | **6.4** | 6.4 | **6.4** | 6.4 | 6.4 | 6.6 |
| Winter | 5.8 | 5.9 | 8.7 | 8.9 | 9.6 | 5.8 | 5.8 | 5.7 | 5.8 | **5.5** | **5.6** | 5.8 | 6.1 |

[a]The parameters are obtained by calibration on the entire period, separately for each season. The model indices refer to the number before the parameterization in Table 4. The best two values of each season are printed in bold.

[28] To investigate the seasonal differences in model parameters and the importance of the seasonal recalibration, the parameters fitted for one season (e.g., spring) are used for the other seasons. The resulting RMSEs are then compared with those obtained with the parameterization fitted on the right season.

[29] Finally, we test the transferability in space of the calibrated parameterizations by applying them to the four other sites located in high alpine areas (see Figure 1 and section 2). At these sites, air temperature and vapor pressure are measured and cloud cover is estimated from measured and potential incoming shortwave radiation in the same way as at T1.

### 3.5. Impact of Parameterizations on Energy Balance Modeling

[30] To assess the importance of the longwave radiation parameterizations on models of glacier melt, we include the best and worst all-sky emissivity models in an energy-balance melt model applied at the point scale. We not only run the model with the optimized parameters but also test the parameterizations with the original parameters (Table 5). The energy balance model is applied at the so-called Central AWS on Haut Glacier d'Arolla for the summer period 2001 (Figure 1 and Table 1).

[31] The model is a two-layer surface energy-balance model that has been developed and tested on Haut Glacier d'Arolla [*Carenzo et al.*, 2009; *Pellicciotti et al.*, 2009, 2011] based on a previous modeling approach by *Brock and Arnold* [2000]. It requires hourly measurements of incoming and reflected shortwave radiation, air temperature, vapor pressure, and wind speed as input as well as information about the measurement site such as slope, aspect, latitude, longitude, and elevation. The aerodynamic roughness length needs to be specified and is taken from *Carenzo et al.* [2009]. Incoming longwave radiation is computed. We test two approaches: (i) combination of Dilley B for clear-sky with the Unsworth cloud correction (best approach, see section 4.2) and (ii) combination of the clear-sky emissivity of Swinbank and the Bolz cloud correction, also used by *Ohmura* [1981] (one of the worst approaches, see section 4.2). The Swinbank and Bolz combination is also tested with the parameters by *Ohmura* [1981], as they have been extensively used in energy balance modeling [*Arnold et al.*, 1996; *Brock et al.*, 2000b; *Brock and Arnold*, 2000].

[32] Outgoing longwave radiation is computed using the Stefan-Boltzmann law with a surface emissivity of 1. Surface temperature is calculated internally by the model. The turbulent sensible and latent heat fluxes are estimated using the bulk aerodynamic method [see *Brock and Arnold*, 2000; *Pellicciotti et al.*, 2008 for details]. The energy available for melt is calculated as the residual of all other terms from the surface energy balance and converted into water equivalent using the latent heat of fusion [*Brock and Arnold*, 2000].

## 4. Results

### 4.1. Clear-Sky Parameterizations

[33] Calibration of the clear-sky parameterizations on the entire data set at T1 yields the best results with Dilley A and Dilley B (Table 6). It is especially remarkable that this holds for all seasons (Table 6). The model performance in the four seasons is also equally good. However, most parameterizations are similarly good when the root mean square error (RMSE) is calculated for the calibration period (Table 6). The MBE is close to zero for all parameterizations and the modeled standard deviation is comparable to the standard deviation of the measurements at clear-sky conditions. For

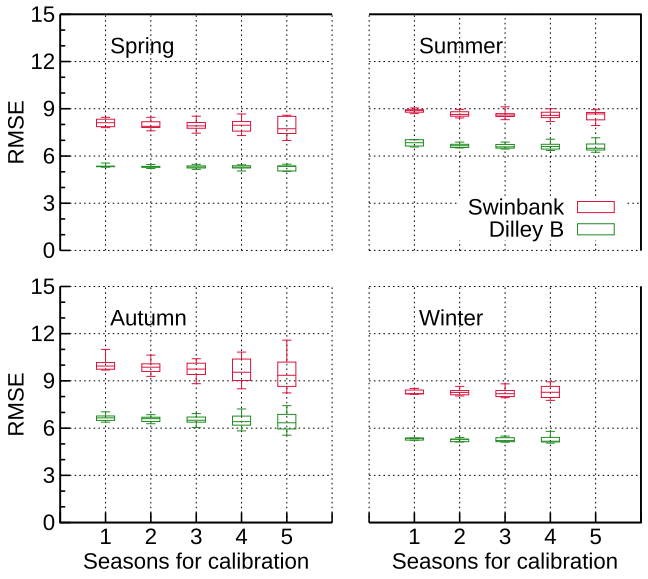


**Figure 3.** The RMSE (W m$^{-2}$) obtained in cross-validation for the Dilley B (one of the best) and the Swinbank (one of the worst) clear-sky parameterizations. Calibration is carried out for spring, summer, autumn, and winter in periods of different length (1–5 years, all possible combinations taken) and the RMSE is computed for the remaining periods. The whiskers denote the maximum and minimum RMSE, the box top is the 75th quantile, the bottom the 25th quantile, and the line in the box is the median of all runs.

**Table 7.** Optimal Parameter Set for the Three Best Clear-Sky Parameterizations Idso81, Dilley A, and Dilley B Calibrated on the Whole Clear-Sky Data Set at T1 for the Four Seasons Separately[a]

| | Parameter | | |
|---|---|---|---|
| Idso81 | a (-) | b ($Pa^{-1}$) | c (K) |
| Spring | 0.65710 | $8.7669 \cdot 10^{-7}$ | 1548.2 |
| Summer | 0.69938 | $1.2034 \cdot 10^{-4}$ | $7.3948 \cdot 10^{-5}$ |
| Autumn | 0.67286 | $3.0727 \cdot 10^{-6}$ | 1112.8 |
| Winter | 0.63394 | $3.1654 \cdot 10^{-8}$ | 2521.5 |
| Original | 0.7 | $5.95 \cdot 10^{-7}$ | 1500 |
| Dilley A | a (-) | b ($K^{-1}$) | c ($m\ kg^{-0.5}$) |
| Spring | 1.1015 | –0.63603 | 0.75670 |
| Summer | 0.0056078 | 0.53034 | 0.54598 |
| Autumn | 0.79242 | –0.27830 | 0.60377 |
| Winter | 1.3846 | –0.95602 | 0.82876 |
| Original | 2.232 | –1.875 | 0.7356 |
| Dilley B | a ($m^2\ W^{-1}$) | b ($m^2\ W^{-1}\ K^{-6}$) | c ($m^3\ kg^{-0.5}\ W^{-1}$) |
| Spring | 44.830 | 142.83 | 99.857 |
| Summer | 31.967 | 163.43 | 75.377 |
| Autumn | 45.450 | 145.71 | 85.612 |
| Winter | 50.522 | 128.80 | 116.27 |
| Original | 59.38 | 113.7 | 96.96 |

[a]The original parameters are taken from *Idso* [1981] and *Dilley and O'Brien* [1998], respectively.

Dilley B, the standard deviations of modeled incoming longwave radiation are 29, 21, 23, and 20 $W\ m^{-2}$ for spring, summer, autumn, and winter, respectively, while the standard deviation of the observed radiation is 30, 22, 24, and 21 $W\ m^{-2}$, respectively.

[34] If we validate the parameterizations on the seasons which are not used for calibration (cross-validation), the Dilley B parameterization gives the best results (Figure 3), but the difference between most parameterizations is small. Only the parameterizations which do not include vapor pressure (such as Swinbank) perform significantly worse (Table A1 in the Appendix). The other parameterizations are very robust in time as the accuracy is independent of the period which is used for fitting the parameters to the data. The RMSE of Dilley B is shown in Figure 3 for cross-validation on 1–5 years, together with the RMSE of the Swinbank parameterization for comparison. Compared to Dilley B, the Swinbank clear-sky parameterization exhibits a higher RMSE and a slightly larger scatter between the different model runs. In cross-validation, the MBE is close to zero for all parameterizations. The optimal parameter sets for the best three clear-sky parameterizations obtained from calibration with the entire period of record are shown in Table 7.

### 4.2. All-Sky Parameterizations

[35] The combinations that reproduce the all-sky data best are Dilley A, Dilley B, and Idso81 for clear-sky atmospheric emissivity with the Unsworth or Lhomme cloud corrections. Dilley B and Unsworth are also recommended in *Flerchinger et al.* [2009], although they did not include glacierized environments. For the whole period at T1, this approach results in an RMSE of 26 $W\ m^{-2}$. For comparison, the RMSE of all parameterizations for every season at T1 is summarized in Table A1 of the Appendix. The optimal parameters of the two best parameterizations obtained from calibration on the entire data set for each season are listed in Table 8.

[36] Cross-validation is conducted in the same way as for the clear-sky parameterizations. Most parameterizations prove robust when validated on other periods than those used for calibration. The Swinbank and Bolz combination, however, results in single combinations with significantly worse RMSEs in spring (Figure 4).

[37] The importance of seasonal calibration of model parameters is shown in Table 9. As an example, we show the RMSEs of the combination of Dilley B for clear-sky conditions with the Unsworth cloud correction applied to each of the four seasons with both the parameters calibrated for that season and with the optimal parameters of the three remaining seasons (Table 9). It is evident that the error increases when parameters from different seasons are used. Some seasons' parameters seem to be less appropriate than others, however. The parameters obtained from autumn and winter seem to be most universal, while in spring longwave radiation cannot be modeled with other parameters and the spring parameters do not work for any other season.

[38] Figure 5 shows the time series of measured incoming longwave radiation together with the results of the Dilley B parameterization combined with the Unsworth cloud correction (one of the best combinations) as well as the Swinbank clear-sky parameterization combined with the Bolz cloud correction for selected sub-periods in each season. The Swinbank parameterization combined with the Bolz cloud correction is shown here as an example of a badly performing combination. We show 10 days for every season to emphasize differences in the mean values and variability. In general, the calibrated parameterizations reproduce the measured incoming longwave radiation quite well. Modeled radiation can reproduce well both the mean values and the variability, which are highest in spring and autumn (Table 3). An exception is winter, because no cloud-cover information is available. In this month, the results of two simulations are shown in Figure 5, one with a constant cloud over of 1 and the second with a cloud cover of 0. The parameters of the cloud correction are taken from those fitted in autumn. In winter, the measured incoming longwave radiation varies between the two cases, which indicates that the parameterizations might work well if a cloud-cover estimate was available. In all seasons, the difference between the two model combinations is small, but the Dilley B and Unsworth combination performs slightly better.

**Table 8.** Optimal Parameters of the Two Best Cloud Corrections Obtained From Calibration on the Entire Data Set for Each of the Three Seasons at T1[a]

| | Cloud Correction | | | |
|---|---|---|---|---|
| | Unsworth | | Lhomme | |
| Season | a (-) | b (-) | a (-) | b (-) |
| Spring | 4.1861 | –2.68470 | 1.0539 | 0.37824 |
| Summer | –1.9323 | 1.77900 | 1.0139 | 0.31509 |
| Autumn | 2.1989 | –1.43380 | 1.0259 | 0.27120 |
| Original | –0.84 | 0.84 | 1.07 | 0.34 |

[a]The calibrated Dilley B parameterization is used to model the clear-sky emissivity. The original parameters are taken from *Unsworth and Monteith* [1975] and *Lhomme et al.* [2007], respectively.

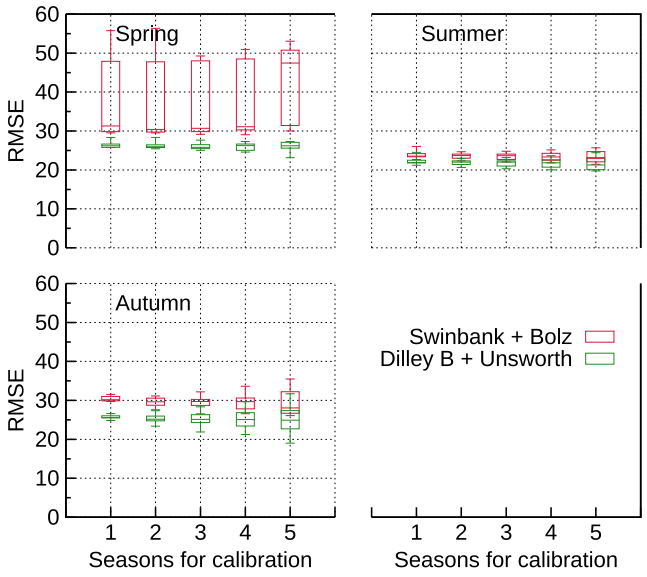


**Figure 4.** The RMSE (W m$^{-2}$) obtained in cross-validation for the Dilley B parameterization combined with Unsworth as well as Swinbank combined with Bolz. Parameters are calibrated for spring, summer, and autumn for periods of different length (1–5 years, all possible combinations) and the RMSE is computed for the remaining period. Winter is not shown as the all-sky parameterizations could not be fitted in this season due to the lack of cloud-cover information. The whiskers denote the maximum and minimum obtained RMSE, the box top is the 75th quantile, the bottom the 25th quantile, and the line in the box is the median of all runs.

### 4.3. Transferability in Space

[39] The calibrated all-sky parameterizations are tested on four validation sites. The comparison of measured and modeled incoming longwave radiation reveals larger errors than at T1 (Table A2 in the Appendix). The parameterizations that perform best, however, remain the same. At T2, the best parameterization is the combination of Dilley B and Unsworth. However, the performance is lower than at the calibration site T1. The corresponding RMSE is 36 W m$^{-2}$, while the mean of all parameterizations is an RMSE of 40 W m$^{-2}$ (Table A2 in the Appendix). These errors are larger than at T1, which is a result of an overestimation of incoming longwave radiation (Figure 6). The MBE for the validation at T2 is 10 W m$^{-2}$ for the combination Dilley B and Unsworth. The large observed variability (standard deviation of almost 60 W m$^{-2}$ computed over the entire data set at T2) is not reproduced by any parameterization. The model combination of Dilley B and Unsworth yields a standard deviation of 45 W m$^{-2}$, which is the second highest of all model combinations. The peaks are well reproduced on average and in all seasons, while overestimation is evident during periods of low incoming longwave radiation, mainly on clear-sky days (Figure 6).

[40] At Haut Glacier de Tsa de Tsan, results are similar to T1. The RMSE for the whole period is in the same range as for T1 (Table A2 in the Appendix). The lowest RMSE is again produced by the combination Dilley B and Unsworth (25 W m$^{-2}$), which suggests that the parameterization is robust not only in time (results of cross-validation above) but also in space. The MBE is negative for all model combinations, (e.g., –9 W m$^{-2}$ for Dilley B and Unsworth). This means that incoming longwave radiation is underestimated at Tsa de Tsan. The observed standard deviation is only 38 W m$^{-2}$, which may explain the good performance of the parameterizations. The data, however, include only one season, which might not be representative.

[41] The third validation site is the AWS Cime Bianche. Results of all parameterizations for incoming longwave radiation reveal a poor performance and only moderate agreement with measured radiation. The best combination is Dilley B and Unsworth with an RMSE of 41 W m$^{-2}$, while the mean of all parameterizations is an RMSE of 47 W m$^{-2}$ (Table A2). The MBE is in the range of 20 W m$^{-2}$ for most parameterizations and the standard deviation is largely underestimated, in agreement with results at T2. All parameterizations strongly overestimate the incoming longwave radiation.

[42] The Miage station lies furthest from T1. The results are comparable to those of Cime Bianche and T2, with incoming longwave radiation being overestimated by all parameterizations. This leads to an RMSE of 39 W m$^{-2}$ for the best parameterization (Idso69 clear-sky parameterization combined with Unsworth cloud correction) (41 W m$^{-2}$ for the combination Dilley B and Unsworth). The MBE is around 20 W m$^{-2}$ for most combinations. Also at this station, the parameterizations strongly underestimate the observed variability. The measured data have a standard deviation of about 45 W m$^{-2}$, while the standard deviation obtained with all the parameterizations ranges between 22 W m$^{-2}$ (Swinbank combined with Unsworth) and 32 W m$^{-2}$ (the combination Idso81 with Kimball).

### 4.4. Implementation in an Energy-Balance Melt Model

[43] We include in the energy balance model the parameterization Dilley B for the clear-sky emissivity combined with the Unsworth cloud correction as the best all-sky parameterization, and the combination of the clear-sky emissivity of Swinbank and the Bolz cloud correction, as one of the poorest performing models, with both recalibrated and original parameters. The latter is also tested with the parameters from *Ohmura* [2001], derived for the Arctic spring and summer.

**Table 9.** The RMSE (W m$^{-2}$) of the Dilley B Clear-Sky Parameterization Combined With the Unsworth Cloud Correction for Every Season Separately When the Parameters Are Calibrated on One Season and Applied to All Seasons for the Entire 6 Year Period[a]

| Calibration Season | Season the Model Is Applied to | | | |
|---|---|---|---|---|
| | Spring | Summer | Autumn | Winter |
| Spring | **25.8** | 29.3 | 31.5 | 48.7 |
| Summer | 30.0 | **21.5** | 28.9 | 59.9 |
| Autumn | 33.9 | 21.4 | **24.8** | 28.9 |
| Winter | 29.2 | 22.1 | 24.5 | **30.1** |

[a]In bold are the results with the parameters optimized for the season they are applied to. For winter, only the clear-sky parameterizations could be fitted and the cloud correction parameters are taken from the fitting to the autumn data; for the application of the parameterizations to winter data, a constant cloud cover of 1 is used.

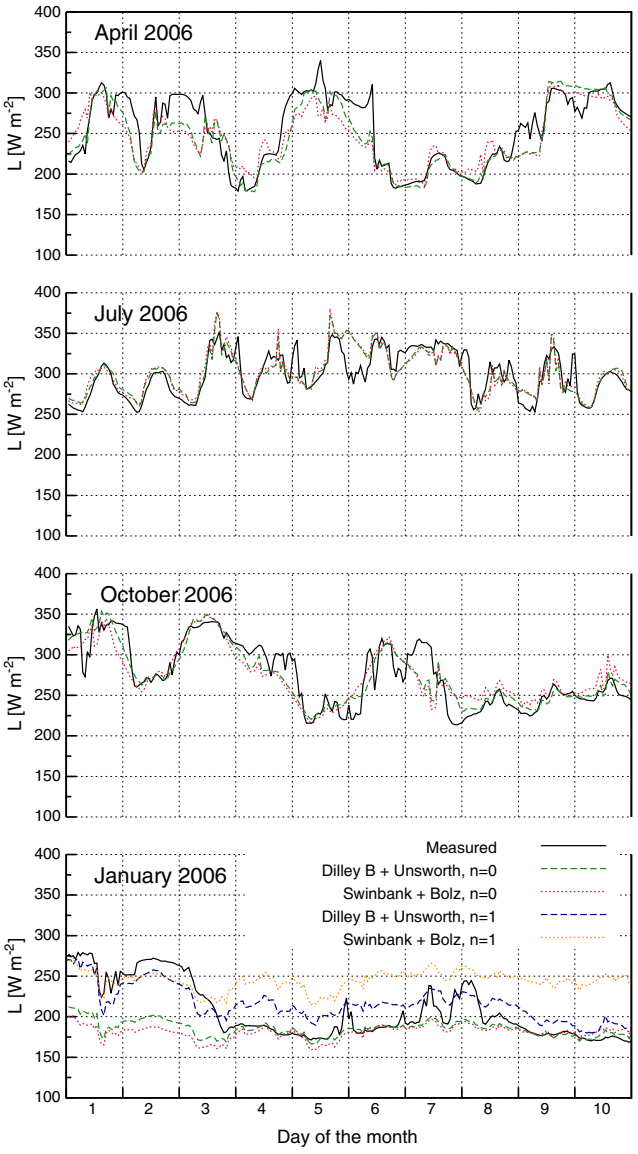


**Figure 5.** Time series of measured incoming longwave radiation at T1 together with simulated radiation from the recalibrated parameterizations by Dilley B combined with Unsworth and Swinbank combined with Bolz, for 10 days of each season in the year 2006. In winter, the clear-sky parameterization is applied once for a constant cloud cover of 0 and once for a cloud cover of 1, as no cloud-cover information is available.

[44] The modeling period is from 23 July to 12 September 2001. The total sum of melt is 1307 mm (25.9 mm $d^{-1}$) for the Dilley B and Unsworth combination with original parameters (Tables 4 and 5), 1466 mm for the calibrated Dilley B and Unsworth combination, 1183, 1303, and 1472 mm for the Swinbank and Bolz combination using the original parameters, the parameters from *Ohmura* [2001], and the calibrated parameters, respectively. Cumulative melt simulated with the five energy balance model variants over the entire period is shown in Figure 7.

[45] It is evident that both parameterizations, once recalibrated for T1, result in similar cumulative melt and agree best with the stake readings (Figure 7). As the calibration tends to minimize the disagreement between the mean value of modeled and measured incoming longwave radiation, both calibrated models show a similar mean behavior. What makes the combination Dilley B and Unsworth performing better than the combination Swinbank and Bolz is its ability to reproduce the variations in longwave radiation, which are not so important for cumulative melt. However, the energy balance model simulations with the original

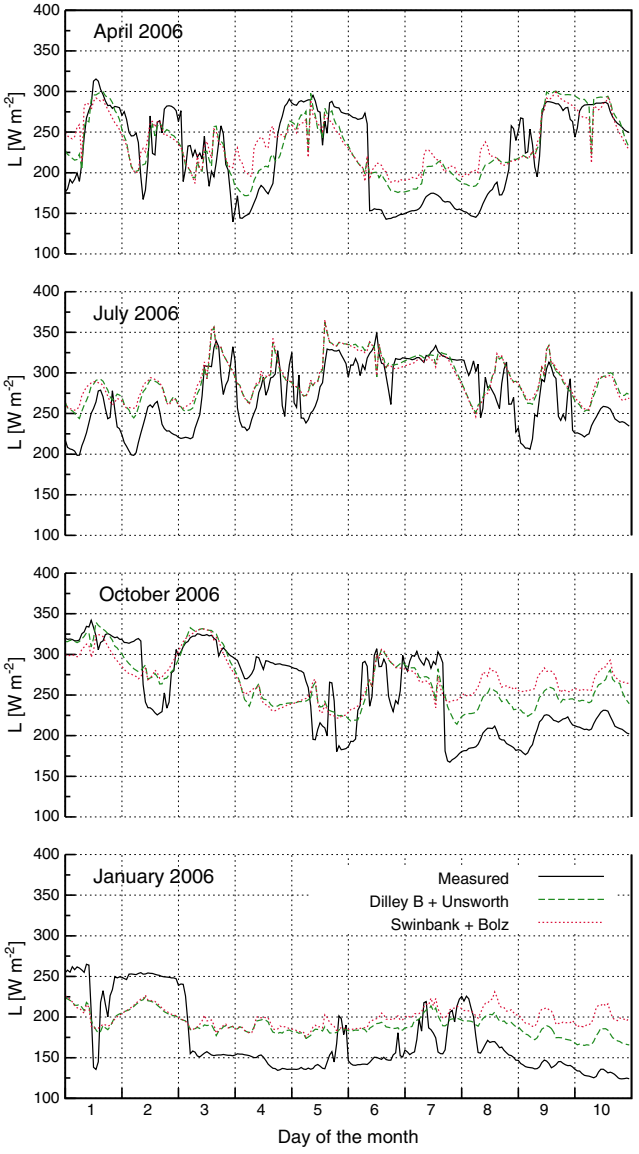


**Figure 6.** Time series of measured incoming longwave radiation at the validation station T2 and results from the Dilley B clear-sky parameterization combined with the Unsworth cloud correction (best parameterization in calibration) and Swinbank clear-sky parameterization combined with Bolz cloud correction (one of the worst combinations in calibration), all calibrated at T1, for 10 days per season, for the year 2006.

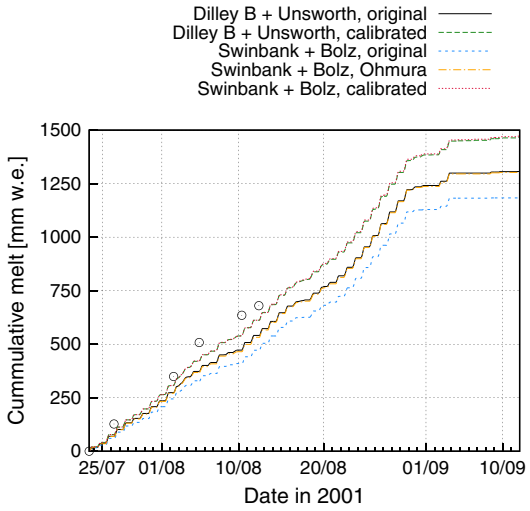


**Figure 7.** Cumulative melt simulated by the energy balance model at Haut Glacier d'Arolla central AWS in summer 2001, together with readings at one ablation stake (circles). The lines indicate energy balance simulations with different longwave radiation parameterizations with the original and calibrated parameter set, see text for more details.

parameters result in significantly lower melt rates for both parameterizations. At the end of the ablation season, the difference in total melt between the lowest and the highest estimate is about 20%. This demonstrates that melt rates calculated with an energy balance model strongly depend on the calibration of the parameters of the longwave radiation model. This finding is supported by the results from *Greuell and Smeets* [2001] who concluded that the incoming longwave radiative flux is the largest source of uncertainty in point energy balance melt modeling.

## 5. Discussion

### 5.1. Performance of Different Parameterizations

[46] In this work, we have tested a large number of empirical parameterizations. The best model in our intercomparison of the clear-sky parameterizations is the Dilley B parameterization. This result is in agreement with those of *Flerchinger et al.* [2009] and *Marthews et al.* [2012], who also found that this was the best clear-sky parameterization, which seems to confirm our results for different, mainly low land locations.

[47] *Dilley and O'Brien* [1998] suggested their two parameterizations (A and B, respectively) as an advancement over the simpler approaches that use screen temperature and water vapor pressure. They argued that precipitable water should be used instead of vapor pressure, based on previous evidence by *Swinbank* [1963], *Idso and Jackson* [1969], *Deacon* [1970], *Brutsaert* [1975], and *Prata* [1996]. *Swinbank* [1963] parameterization, in particular, which uses screen air temperature alone and assumes a dependency of longwave radiation on $T^6$, was based on the argument that screen temperature is a better indicator of the mass of radiatively active water vapor than the surface vapor pressure. However, *Idso and Jackson* [1969], *Brutsaert* [1975], and *Prata* [1996] all recognized that precipitable water is the main indicator of the mass of radiatively active water vapor. The controversy introduced by *Swinbank* [1963] is discussed also in *Dilley and O'Brien* [1998], and analysis of atmospheric profiles made available by numerical weather prediction models, radiosondes, or satellite sensors might contribute to make some more clarity.

[48] *Dilley and O'Brien* [1998] suggested two parameterizations (A and B), of which Dilley B is a simplification of the original Dilley A. Both parameterizations are the only two clear-sky parameterizations which combine a temperature-dependent and a humidity-dependent term in an additive manner (Table 4). The two terms were derived from physically based considerations to represent the optical thickness of a grey body [*Dilley and O'Brien*, 1998]. This might explain their better performance over other approaches. One has to consider, however, that in the original paper, *Dilley and O'Brien* [1998] used precipitable water extracted from a subset of the TIGR data set [*Chedin et al.*, 1985] and not computed with the simple approach we used based on screen temperature and surface vapor pressure (equation (2)). The authors calculated the model parameters and model performance against profiles of longwave radiation calculated with the detailed radiative transfer model LOWTRAN7 and obtained high agreement. They also showed, however, that the error was higher for high differences between the temperature of the surface layer and that of the layer immediately above [Figure 2 of *Dilley and O'Brien*, 1998]. They therefore concluded that the accuracy of the parameterizations will be affected by low-level temperature inversions. They also suggested that under conditions of strong inversion, the parameterizations would likely underestimate longwave radiation and concluded by recommending that for such situations, models of incoming longwave radiation should include data about the vertical profiles of temperature. This is a warning that should be taken into account and will be discussed more in section 5.2 below.

[49] Our second main result is that when calibrated and validated at the same station, several parameterizations model the incoming longwave radiation with an acceptable accuracy. This is also in agreement with previous findings [e.g., *Sedlar and Hock*, 2009; *Gubler et al*., 2012; *MacDonell et al*., 2013]. However, a distinction in model performance seems to be evident between clear-sky parameterizations that include the vapor pressure of the atmosphere and those which do not. The parameterizations that do not include humidity in the clear-sky emissivity (Swinbank, Idso69, and Maykut) perform significantly worse than the other parameterizations (Table 6). This finding matches with other studies [e.g., *Hatfield et al*., 1983; *Flerchinger et al*., 2009].

[50] As regards the cloud parameterizations, cloud corrections which do not include a clear-sky emissivity (Marshunova and König-Langlo) perform significantly worse than other cloud corrections (Table A1). Also the Kimball cloud correction should be used with caution, as it is not robust if all parameters are fitted. It is more useful when only two parameters are fitted to the data as it was done in this work.

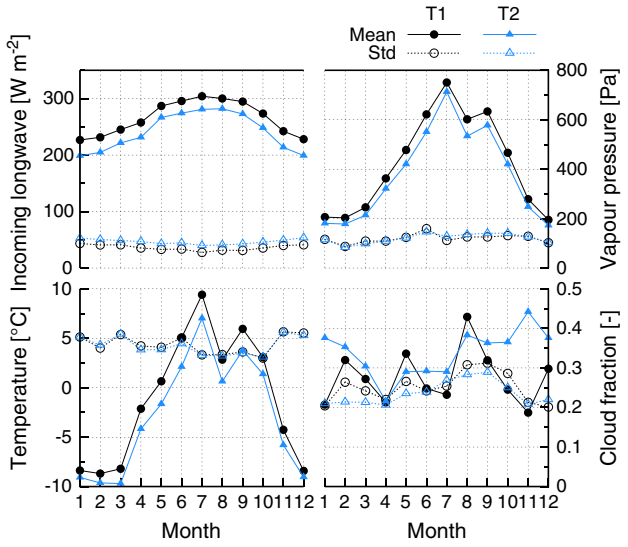


**Figure 8.** Measured incoming longwave radiation, air temperature, vapor pressure, and calculated cloud cover at AWS T1 (black) and T2 (blue), mean values and standard deviations for each month in the common period (26 November 2005 to 28 June 2007).

### 5.2. Model Transferability

[51] A clear result of our work is that calibration of the parameterizations is more important than the choice of the models, since several parameterizations performed almost equally well once recalibrated for one site. When validated at the four validation sites, the parameterizations calibrated at T1 resulted in large differences in model performance. This seems to indicate that the spatial variability of incoming longwave radiation cannot be explained only on the basis of 2 m meteorological variables such as air temperature, humidity, and the simple cloud-cover estimate commonly used, as it was pointed at already in the early studies on longwave irradiance [e.g., *Swinbank*, 1963]. *Swinbank* [1963] noted that "the wide variation with locality" of the empirical parameters of both Brunt and Ångström parameterizations was a "disturbing feature tending to throw doubts on the physical basis of the formulations." As recognized also by *Swinbank* [1964], the scatter in parameters and model performance from one site to the other could be associated to differences in the atmospheric profiles of air temperature and moisture. *Swinbank* [1964] noted that "when there is a strong temperature gradient at screen level these formulae, as indeed any based on single measurements at screen level, are likely to be in error." Therefore, models based only on these measurements fail to reproduce incoming longwave radiation at other sites than the calibration stations. Three factors might contribute to explain the differences in model performance and parameters at the sites.

[52] The first factor is the atmospheric profile of air temperature and humidity, as recognized already [e.g., *Swinbank*, 1964; *Dilley and O'Brien*, 1998]. The longwave radiation models tested are based on measurements of 2 m air temperature and humidity. However, longwave radiation is emitted by the entire atmospheric boundary layer (ABL) above the surface [*Ohmura*, 2001]. Especially in the lowest few hundred meters, the effective temperature for the emitted atmospheric radiation is governed by the temperature lapse rate (LR) in the ABL. Differences in the stratification of the atmosphere and the LRs in the ABL at the various locations might therefore explain the differences in model parameters and performances. Our data sets show indications of such variability in temperature profiles at T1 and T2, which are both located close to Haut Glacier d'Arolla. The temperature time series at the two locations provide indications that the stratification at the two sites might be different, as T1 and T2 have two temperature regimes that cannot be explained only by elevation differences. T1 is located 490 m lower than T2 which would result in a mean temperature difference of 3.2°C using a standard moist adiabatic LR of 0.0065°C $m^{-1}$. However, measured air temperatures are on average only 0.6°C (December) to 2.9°C (June) warmer at T1 compared to T2 (Figure 8). This can be explained by a combination of reasons. The first is the effect of the glacier, and glacier wind especially, which extends beyond the glacier surface [*Greuell and Böhm*, 1998] and causes temperatures in the pro-glacial valley to be colder than they would be at the same elevation [*Dadic et al.*, 2008]. T1 is located about 1.5 km from the glacier terminus. In this location, cold glacier winds occur frequently, reducing the average air temperature at 2 m height [*Dadic et al.*, 2008]. The second reason is the topographic shading, which is strong especially in winter, when the measured temperature at T1 is very low compared to the other stations (see Figure 2). As the 2 m temperature at T1 is colder than it would be without the glacier influence, it is possible that inversion occurs in the atmosphere above it. If the temperature in higher atmospheric layers is warmer, the relation between air temperature at 2 m and incoming longwave radiation is likely to be biased and the calibrated parameters will be tuned toward the cold 2 m temperature. In contrast to T1, T2 reveals higher than average (for the given elevation) temperatures because it is located in a topographic bowl that warms up during the day and also supplies shelter from strong winds [*Dadic et al.*, 2008]. This difference to T1 is likely one of the major reasons why the models calibrated at T1 overestimate the incoming longwave radiation at T2, and at the other stations except for Tsa de Tsan. Tsa de Tsan is the only station located on a glacier, except for the debris-covered Miage Glacier. Thus, the air temperature at Tsa de Tsan is influenced by the cooling effect of the underlaying ice and possibly also by cold glacier winds. Differences in the atmospheric profiles might affect not only the mean values but also the variability of the record (Figure 8), which is quite different at the five AWSs and at T1 and T2 in particular. Due to the different measurement periods, the data sets are difficult to compare, but the standard deviations indicate that the incoming longwave radiation is more variable at T2 and Cime Bianche compared to T1 (Figure 8). We suggest that the effect of different profiles of air temperature and lapse rates in the overlaying atmosphere is the most probable reason why it is important to recalibrate parameters also for every season.

[53] The differences in structure and radiative properties of the atmosphere between the stations are related to the weather conditions. The mean monthly apparent emissivity was calculated from measurements of incoming

longwave radiation and air temperature at 2 m at all five AWSs for clear-sky hours and not-clear-sky hours separately (Figure 9). As the common period of all stations is short (Table 1), all data are shown for each station. As it is to expect, the mean emissivity on clear-sky hours is significantly less than on hours with some cloud cover at all stations (Figure 9). However, variability is very different between the stations. Figure 9 shows in particular that differences between all stations are large for clear-sky conditions, but not so much (especially for T1 and T2) for cloudy conditions. This agrees well with the argument above, as a cold glacier wind is more likely to develop under clear-sky conditions [*Stenning et al.*, 1981; *Greuell and Böhm*, 1998; *Petersen et al.*, 2013]. Furthermore, the influence of terrain radiation on the sensor signal is larger under clear-sky conditions (see below).

[54] A second factor that might explain the differences in calibrated model parameters and model performance between seasons and sites is the cloud cover. The mean daytime cloud cover in the summer month June to September exhibits relatively large variations between the five sites, with the highest values at T1 and T2 (both 0.3), followed by Tsa (0.26), Miage (0.25), and Cime (0.22). The low value at Cime might explain the relatively low value of measured incoming longwave radiation shown in Figure 10a. It has to be considered that cloud cover is estimated on the basis of incoming shortwave radiation. Important characteristics such as the average height of the clouds above the sensor, the optical thickness, and temperature of the cloud base are not taken into account, but affect the longwave flux emitted by clouds [e.g., *Bolz*, 1949; *Unsworth and Monteith*, 1975; *Niemelä et al.*, 2001; *Gröbner et al.*, 2009] and therefore the parameters' calibration. Unfortunately, the influence of different cloud characteristics cannot be identified in this work as no such data are available and so it is difficult to estimate their importance but the differences in calculated cloud cover above might be an indication of differences also in cloud characteristics. However, given that T1, T2, and Tsa de Tsan are located quite close to each other and the parameters from T1 work well on Tsa but not on T2, it seems that the influence of the temperature lapse rate might be more important than differences in cloud cover. This might not be valid for Cime Bianche and Miage.

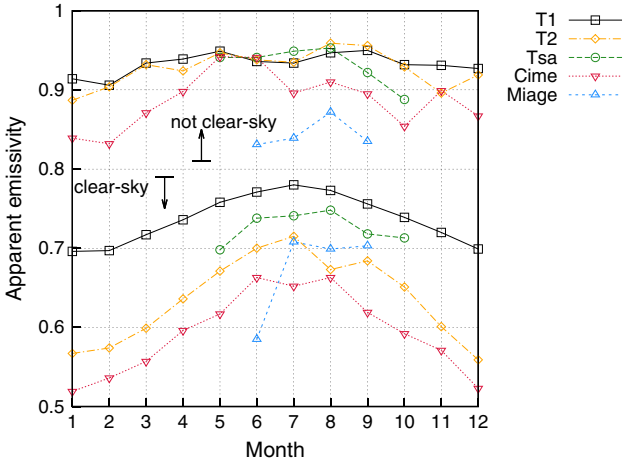


**Figure 9.** Apparent emissivity calculated from measured incoming longwave radiation and air temperature at each automatic weather station for the whole data set. At the bottom are mean values calculated for all clear-sky hours of each month and at the top the mean values for all other data points.

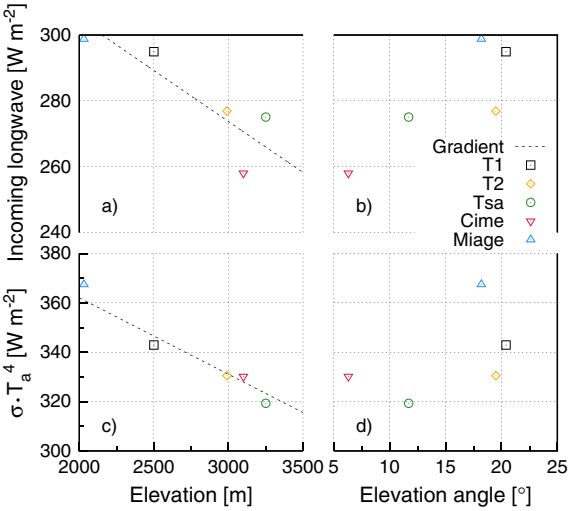


**Figure 10.** Mean measured incoming longwave radiation and calculated black-body radiation from air temperature (equation (1)) for the summer months (June to September) at the five automatic weather stations in relation to the station elevations and the elevation angles of the surrounding terrain; the dashed line is the gradient of incoming longwave radiation with elevation derived by *Marty et al.* [2002] for summer conditions (0.031 W m$^{-2}$ m$^{-1}$).

[55] Terrain-emitted radiation is the third factor justifying differences among sites and seasons in model parameters and performance, especially under clear-sky conditions. As it is not measured at the stations, its influence can only be modeled or estimated from the literature. *Plüss and Ohmura* [1997] investigated the additional radiation from the surrounding terrain compared to the unobstructed sky. For a mean elevation angle of the surrounding terrain ($\alpha$) of 20°, the additional terrain irradiance is below 10 W m$^{-2}$ [*Plüss and Ohmura*, 1997]. We calculated $\alpha$ at all our sites. T1 has the largest $\alpha$ of all five stations, T2 and Miage are similar to T1, while Tsa de Tan and Cime Bianche have a lower $\alpha$ (Table 1 and Figure 10b). $\alpha$ does not provide an explanation of the differences in incoming longwave radiation between T1, T2, and Tsa, but it might be one of the reasons for the low mean values at Cime Bianche (Figure 10a). At this station, the measured incoming longwave radiation is lower than might be expected from the air temperature or elevation and $\alpha$ is the lowest of all sites.

[56] Calculations of the terrain-emitted radiation require surface temperature and emissivity of the slopes. The temperature of the slopes is variable and strongly influenced by exposition and cloudiness. Even a rough estimate would require information on the snow cover of the slopes as this has a large influence on the emissivity and the temperature of the rock surfaces. Therefore, the input data for a model which includes the radiation from the surrounding

slopes would rely on many assumptions, and be affected by uncertainties.

[57] It has been suggested in the literature that elevation is a control on incoming longwave radiation [e.g., *Marty et al*., 2002; *Iziomon et al*., 2003]. We compared the elevation dependency of incoming longwave radiation with the elevation dependency of air temperature, which is the main driver of longwave radiation (Figures 10a and 10c). At our AWSs, the decrease of air temperature with elevation is much clearer than the decrease of incoming longwave radiation (Figures 10a and 10c). The gradient of 0.031 $W m^{-2} m^{-1}$ derived by *Marty et al.* [2002] for summer fits well to the calculated black-body radiation from air temperature (equation (1) and Figure 10c). In comparison with the air temperature data, the incoming longwave radiation shows more scattering (Figure 10a), due to the other factors affecting the sky emissivity discussed above, but the gradient of 0.031 $W m^{-2} m^{-1}$ provides an acceptable fit. This indicates that the elevation dependency of incoming longwave radiation in our data set can largely be explained by the temperature variation, but the variability of the residuals cannot fully be explained with the information available in this study.

### 5.3. Importance of Accurate Estimate of Cloud Cover

[58] Our study has also demonstrated that it is important to reasonably estimate the cloud cover. The selection of the clear-sky data from measured incoming longwave radiation is more accurate than a previously tested approach which considered the difference between the potential and the measured incoming shortwave radiation. With this approach, the best parameterizations resulted in an RMSE of about 20 $W m^{-2}$ for clear-sky conditions instead of 6 $W m^{-2}$ (Table 6) in the current approach. The main advantage of the selection based on longwave data is the accurate classification of nights, when the cloud cover cannot be calculated using shortwave radiation.

[59] However, even in the case of the less carefully selected data set for calibration of the clear-sky parameterizations, Dilley B was the best model. It seems to be most robust with regard to cloudy observations in the calibration data set. If no cloud observations are available, this parameterization can be fitted to the all-sky data with the best results.

## 6. Conclusions

[60] We have analyzed 13 parameterizations of clear-sky atmospheric emissivity combined with eight cloud corrections for modeling incoming longwave radiation. The four seasons were treated separately to both identify the intra-annual variability and test the seasonal differences in parameters and model performances. The parameterizations were tested for robustness and transferability in time and space. We carried out a cross-validation in time by calibrating model parameters for a varying number of years from one to five, using all possible combinations, and validating the model performance on the remaining years. We used the RMSE, MBE, and standard deviation as measures of agreement between simulations and observed radiation. We conducted this analysis at hourly resolution at one site on Haut Glacier d'Arolla. To assess transferability in space, we validated the parameterizations against observations of longwave radiation at four different sites for which data are available.

[61] Our conclusions are as follows:

[62] 1. The best all-sky parameterization is the combination of Dilley B for the clear-sky emissivity and the Unsworth cloud correction. This holds for all four seasons. This parameterization is also robust in time, being the one with the smallest errors also when the data set is split into a calibration and a validation set. The RMSE for the whole period at the calibration station T1 is 26 $W m^{-2}$, which is in the range of the measurement uncertainty. This combination is also one of the best at all validation stations. Our results are in agreement with those by *Flerchinger et al.* [2009], who also found that this combination was the best out of 13 clear-sky parameterizations and 10 cloud corrections. The study by *Marthews et al.* [2012] also show that Dilley B performs best of several clear-sky models. However, several model combinations are almost equally good, starting from Idso81 and Dilley A clear-sky parameterizations (our second and third best models) and the Lhomme cloud correction. This finding is in agreement with *Sedlar and Hock* [2009], *Gubler et al.* [2012], and *MacDonell et al.* [2013], who also identified the parameter fit to be more important than the choice of model. Even if the parameterizations are fitted on the data of only 1 year, the modeling error is acceptable.

[63] 2. Seasonal calibration seems important at the locations examined in this study, as the longwave radiation patterns are distinct among the four seasons (Figures 5, 6, and 10). The parameters of all models are empirical [*Dilley and O'Brien*, 1998] and include implicitly the influence of factors such as the average temperature lapse rate in the atmospheric boundary layer, the cloud characteristics, and amount of radiation emitted by the terrain. These parameters seem to be stable at one location in one season (e.g., summer), but not for different seasons. As a result, the error increases substantially when parameters optimized for one of the seasons are applied to another season.

[64] 3. Spatial recalibration seems to be as important as seasonal recalibration. This is due to the fact that all parameterizations are empirical [e.g. *Swinbank*, 1964]. Transferring the calibrated Dilley B and Unsworth parameterization to the four validation stations available for this study results in RMSE of 25 (Tsa de Tsan), 36 (T2), 41 (Miage), and 41 $W m^{-2}$ (Cime Bianche). The Dilley B clear-sky parameterization combined with the Unsworth cloud correction is among the best parameterizations at all stations. The large RMSE at three of the four stations can mainly be attributed to an overestimation of the incoming longwave radiation combined with an underestimation of the variability. We argue that this is likely due to differences in three main factors: (i) air and moisture profiles in the atmospheric boundary layer and related lapse rates, (ii) cloud characteristics, and (iii) radiation emitted by the terrain. We suggest that the former is likely the most important. Future work should include the development of simple models to include terrain-emitted radiation into models of incoming longwave radiation. More work should also be devoted to quantify the relative importance of the three factors. None of these effects

can be represented by 2 m air and humidity only, and their influence thus requires recalibration of model parameters. Therefore, transferring models of incoming longwave radiation to different stations from those for which they were calibrated, even if in the same large climatic region, leads to large uncertainties, at least in high alpine environments. Further work should be devoted to testing this result in other areas and with a larger observational network. More importantly, however, we think that the effect of the atmospheric profiles of temperature and moisture on the longwave irradiance and on model parameters should be investigated, as it was already pointed out by *Swinbank* [1963] and *Dilley and O'Brien* [1998]. This could be analyzed using outputs from atmospheric Limited Areas Models (LAMs) or numerical Weather Prediction Models, which can provide detailed profiles of atmospheric variables at several heights for grids of relatively high spatial resolution (few kilometers).

[65] 4. These results translate into energy balance modeling of glacier surfaces directly. We show that to correctly reproduce cumulative melt at one location on a glacier, the choice of the parameterization is not so important as its recalibration. This is an important result that advises against using parameterizations of longwave radiation taken from literature in studies of glacier energy balance and melt. Our results suggest that uncertainties in modeled incoming longwave radiation might imply high uncertainties in melt modeling of up to 20% of cumulative melt. This result confirms findings by *Greuell and Smeets* [2001] who found that the uncertainty of incoming longwave radiation resulted in an uncertainty in computed net ablation of 2.4 mm water equivalent $d^{-1}$ (3.5–10% of the measured ablation at different AWS).

[66] Although our analysis focuses on high-elevation, glacierized sites, it might be relevant also for different

**Table A1.** The RMSEs (W $m^{-2}$) of Modeled and Observed Data for All Clear-Sky Algorithms Combined With All Cloud Corrections for the Entire Period (2000–2007) at T1[a]

| Cloud Correction | Clear-Sky Parameterization | | | | | | | | | | | | |
|---|---|---|---|---|---|---|---|---|---|---|---|---|---|
| | 1 | 2 | 3 | 4 | 5 | 6 | 7 | 8 | 9 | 10 | 11 | 12 | 13 |
| Spring | | | | | | | | | | | | | |
| 1 | 26.5 | 26.6 | 29.5 | 29.0 | 28.8 | 26.6 | 25.7 | 26.4 | 26.4 | 25.8 | 25.7 | 26.5 | 26.5 |
| 2 | 26.4 | — | — | — | — | — | — | — | — | — | — | — | — |
| 3 | 27.0 | 27.0 | 29.8 | 29.8 | 29.7 | 27.1 | 25.9 | 26.8 | 26.8 | 26.0 | 25.8 | 27.0 | 27.0 |
| 4 | 27.6 | 27.6 | 30.5 | 30.1 | 29.8 | 27.7 | 26.9 | 27.5 | 27.5 | 26.9 | 26.8 | 27.6 | 27.6 |
| 5 | 28.6 | — | — | — | — | — | — | — | — | — | — | — | — |
| 6 | 27.4 | 27.4 | 29.0 | 28.9 | 28.8 | 27.5 | 26.9 | 27.3 | 27.3 | 27.0 | 26.9 | 27.4 | 27.3 |
| 7 | 30.9 | 30.9 | 33.8 | 33.5 | 33.4 | 31.1 | 30.1 | 30.8 | 30.8 | 30.3 | 30.1 | 31.0 | 30.8 |
| 8 | 26.3 | 26.4 | 29.4 | 28.9 | 28.7 | 26.4 | **25.6** | 26.2 | 26.2 | **25.6** | **25.5** | 26.4 | 26.4 |
| Summer | | | | | | | | | | | | | |
| 1 | 21.6 | 21.6 | 23.1 | 22.7 | 22.1 | 21.8 | 21.6 | 21.4 | 21.4 | 21.8 | 21.7 | 21.6 | 21.4 |
| 2 | 21.5 | — | — | — | — | — | — | — | — | — | — | — | — |
| 3 | 21.4 | 21.5 | 21.3 | 21.5 | 22.3 | 21.5 | 21.4 | 21.4 | 21.4 | 21.5 | 21.5 | 21.4 | 21.4 |
| 4 | 21.8 | 21.8 | 23.3 | 22.9 | 22.4 | 22.0 | 21.8 | 21.7 | 21.7 | 22.0 | 21.9 | 21.8 | 21.7 |
| 5 | 22.1 | — | — | — | — | — | — | — | — | — | — | — | — |
| 6 | 21.3 | 21.3 | 22.5 | 22.3 | 22.1 | 21.5 | 21.3 | **21.3** | **21.3** | 21.5 | 21.4 | **21.3** | 21.3 |
| 7 | 22.3 | 22.3 | 23.9 | 23.7 | 23.3 | 22.5 | 22.3 | 22.2 | 22.2 | 22.5 | 22.4 | 22.3 | 22.2 |
| 8 | 21.6 | 21.6 | 23.1 | 22.7 | 22.1 | 21.8 | 21.6 | 21.4 | 21.4 | 21.8 | 21.7 | 21.6 | 21.4 |
| Autumn | | | | | | | | | | | | | |
| 1 | 26.0 | 26.0 | 29.1 | 28.3 | 28.2 | 26.2 | 25.4 | 25.8 | 25.8 | 25.6 | 25.3 | 25.9 | 25.9 |
| 2 | 25.6 | — | — | — | — | — | — | — | — | — | — | — | — |
| 3 | 25.8 | 25.8 | 28.7 | 28.1 | 28.3 | 26.0 | **25.0** | 25.5 | 25.5 | 25.2 | **24.8** | 25.7 | 25.7 |
| 4 | 26.4 | 26.4 | 29.2 | 28.4 | 28.4 | 26.5 | 25.8 | 26.3 | 26.2 | 26.0 | 25.8 | 26.3 | 26.3 |
| 5 | 27.9 | — | — | — | — | — | — | — | — | — | — | — | — |
| 6 | 26.9 | 26.8 | 28.8 | 28.2 | 28.2 | 27.0 | 26.4 | 26.8 | 26.7 | 26.6 | 26.4 | 26.8 | 26.8 |
| 7 | 26.9 | 26.9 | 28.9 | 28.4 | 28.3 | 27.0 | 26.5 | 26.8 | 26.8 | 26.6 | 26.5 | 26.8 | 26.8 |
| 8 | 25.7 | 25.7 | 28.8 | 28.0 | 27.9 | 25.8 | 25.0 | 25.5 | 25.5 | 25.3 | **25.0** | 25.6 | 25.6 |
| Winter | | | | | | | | | | | | | |
| 1 | 43.5 | 43.4 | 50.2 | 48.8 | 48.5 | 44.0 | 41.7 | 43.3 | 43.1 | 42.7 | 42.1 | 43.5 | 43.0 |
| 2 | 38.9 | — | — | — | — | — | — | — | — | — | — | — | — |
| 3 | 34.9 | 36.2 | 59.9 | 59.9 | 59.9 | 36.5 | **30.7** | 34.1 | 34.8 | **31.7** | **30.1** | 35.5 | 35.6 |
| 4 | 50.6 | 50.1 | 55.4 | 54.9 | 54.8 | 50.8 | 48.8 | 50.2 | 50.0 | 49.7 | 49.3 | 50.3 | 49.7 |
| 5 | 59.9 | — | — | — | — | — | — | — | — | — | — | — | — |
| 6 | 59.9 | 59.9 | 59.5 | 59.7 | 59.6 | 59.9 | 59.9 | 59.9 | 59.9 | 59.9 | 59.9 | 59.9 | 59.9 |
| 7 | 59.9 | 59.9 | 59.9 | 59.9 | 59.9 | 59.9 | 59.9 | 59.9 | 59.9 | 59.9 | 59.9 | 59.9 | 59.9 |
| 8 | 44.0 | 43.7 | 50.4 | 49.1 | 49.0 | 44.4 | 41.9 | 43.7 | 43.5 | 43.0 | 42.5 | 43.9 | 43.2 |

[a]The parameters are obtained by calibration on the entire period, separately for each season. For winter, the cloud correction parameters are taken from the fitting on autumn data and a constant cloud cover of 1 is assumed. The model indices refer to the number before the parameterization in Tables 4 and 5 for clear-sky parameterizations and cloud corrections, respectively. The best three values of each season are printed in bold.

**Table A2.** The RMSEs ($W\,m^{-2}$) for All Clear-Sky Algorithms Combined With All Cloud Corrections for the Entire Period (See Table 1 for the Periods at Each Station) at the Four Validation Stations[a]

| Cloud Correction | Clear-Sky Parameterization | | | | | | | | | | | | |
|---|---|---|---|---|---|---|---|---|---|---|---|---|---|
| | 1 | 2 | 3 | 4 | 5 | 6 | 7 | 8 | 9 | 10 | 11 | 12 | 13 |
| T2 | | | | | | | | | | | | | |
| 1 | 38.8 | 38.9 | 42.6 | 42.9 | 42.7 | 38.8 | 38.3 | 38.6 | 38.4 | 38.2 | 38.2 | 38.9 | 38.9 |
| 2 | 38.6 | — | — | — | — | — | — | — | — | — | — | — | — |
| 3 | 36.8 | 37.1 | 42.6 | 48.2 | 41.7 | 36.9 | **36.0** | 36.6 | 36.5 | **35.8** | **35.6** | 37.0 | 37.2 |
| 4 | 38.0 | 38.2 | 41.6 | 41.7 | 41.5 | 38.1 | 37.7 | 37.9 | 37.7 | 37.6 | 37.5 | 38.2 | 38.2 |
| 5 | 45.2 | — | — | — | — | — | — | — | — | — | — | — | — |
| 6 | 39.3 | 39.4 | 43.3 | 43.3 | 43.3 | 39.4 | 38.9 | 39.2 | 38.9 | 38.8 | 38.7 | 39.4 | 39.4 |
| 7 | 39.3 | 39.4 | 42.0 | 42.1 | 42.0 | 39.3 | 39.1 | 39.2 | 39.0 | 38.9 | 38.9 | 39.4 | 39.5 |
| 8 | 39.3 | 39.4 | 43.1 | 43.4 | 43.1 | 39.3 | 38.9 | 39.1 | 38.9 | 38.7 | 38.7 | 39.4 | 39.4 |
| Tsa de Tsan | | | | | | | | | | | | | |
| 1 | 25.4 | 25.4 | 27.5 | 26.3 | 25.9 | 25.4 | 25.2 | 25.1 | 25.2 | 25.4 | 25.2 | 25.4 | 25.2 |
| 2 | 25.3 | — | — | — | — | — | — | — | — | — | — | — | — |
| 3 | 25.0 | 25.0 | 25.4 | 25.9 | 26.5 | 24.8 | 24.7 | 24.9 | 25.0 | **24.6** | **24.5** | 25.0 | 25.0 |
| 4 | 26.0 | 26.0 | 28.0 | 27.0 | 26.7 | 26.0 | 25.8 | 25.7 | 25.8 | 26.0 | 25.8 | 26.0 | 25.8 |
| 5 | 26.5 | — | — | — | — | — | — | — | — | — | — | — | — |
| 6 | 24.8 | 24.8 | 26.5 | 26.0 | 25.9 | 24.8 | 24.7 | 24.7 | 24.7 | 24.7 | **24.6** | 24.8 | 24.7 |
| 7 | 27.7 | 27.6 | 30.2 | 29.4 | 28.9 | 27.8 | 27.5 | 27.4 | 27.4 | 27.7 | 27.5 | 27.7 | 27.5 |
| 8 | 25.7 | 25.7 | 28.0 | 26.9 | 26.7 | 25.7 | 25.5 | 25.4 | 25.4 | 25.7 | 25.5 | 25.7 | 25.6 |
| Cime Bianche | | | | | | | | | | | | | |
| 1 | 45.0 | 45.3 | 49.3 | 50.0 | 50.0 | 44.9 | 45.1 | 44.9 | 44.6 | 44.6 | 44.6 | 45.1 | 45.4 |
| 2 | 45.2 | — | — | — | — | — | — | — | — | — | — | — | — |
| 3 | 42.4 | 43.0 | 50.7 | 57.7 | 49.7 | 42.5 | **42.1** | 42.2 | 42.3 | **41.6** | **41.3** | 42.7 | 43.2 |
| 4 | 44.8 | 45.1 | 48.9 | 49.4 | 49.4 | 44.7 | 44.9 | 44.7 | 44.4 | 44.4 | 44.4 | 44.9 | 45.2 |
| 5 | 53.0 | — | — | — | — | — | — | — | — | — | — | — | — |
| 6 | 46.3 | 46.4 | 50.5 | 50.9 | 51.0 | 46.3 | 46.1 | 46.1 | 45.8 | 45.9 | 45.8 | 46.3 | 46.5 |
| 7 | 46.6 | 46.8 | 49.4 | 49.9 | 50.0 | 46.5 | 46.8 | 46.5 | 46.2 | 46.4 | 46.4 | 46.7 | 46.9 |
| 8 | 46.2 | 46.4 | 50.4 | 51.2 | 51.2 | 46.1 | 46.3 | 46.0 | 45.7 | 45.8 | 45.8 | 46.3 | 46.6 |
| Miage | | | | | | | | | | | | | |
| 1 | 42.6 | 42.6 | 42.4 | 42.2 | 40.2 | 42.5 | 43.0 | 42.4 | 42.3 | 42.5 | 42.7 | 43.1 | 42.4 |
| 2 | 42.8 | — | — | — | — | — | — | — | — | — | — | — | — |
| 3 | 40.9 | 41.0 | **39.4** | **39.2** | **39.5** | 40.8 | 41.1 | 40.9 | 40.9 | 40.8 | 41.0 | 41.2 | 40.9 |
| 4 | 41.8 | 41.8 | 41.9 | 41.5 | 39.7 | 41.7 | 42.2 | 41.6 | 41.5 | 41.8 | 41.9 | 42.2 | 41.6 |
| 5 | 40.4 | — | — | — | — | — | — | — | — | — | — | — | — |
| 6 | 41.8 | 41.8 | 42.0 | 41.7 | 40.2 | 41.8 | 42.0 | 41.6 | 41.6 | 41.8 | 41.9 | 42.1 | 41.6 |
| 7 | 40.1 | 40.2 | 40.2 | 40.1 | 38.8 | 40.1 | 40.4 | 40.0 | 40.0 | 40.2 | 40.3 | 40.4 | 40.1 |
| 8 | 43.1 | 43.1 | 42.7 | 42.5 | 40.5 | 42.9 | 43.5 | 42.9 | 42.8 | 43.0 | 43.2 | 43.6 | 43.0 |

[a]The parameters are obtained by calibration on the entire period at T1, separately for each season. The model indices refer to the number before the parameterization in Tables 4 and 5 for clear-sky parameterizations and cloud corrections, respectively. The best three values of every location are printed in bold.

applications other than melt modeling. Estimation of incoming longwave radiation is relevant for most studies of energy balance and land surface interaction with the atmosphere, including studies of surface evapotranspiration. Reference evapotranspiration is often calculated with the Penman-Monteith equation, recommended by the FAO Manual [*Allen et al.*, 1998]. The authors recommend calculation of net longwave radiation with an empirical approach similar to the combination of clear-sky emissivity by *Brunt* [1932] and the cloud correction by *Lhomme et al.* [2007], which is among the poorly performing parameterizations in our study. We suggest that also for evapotranspiration studies the applicability of the incoming longwave radiation calculation and the possible errors should be verified against data.

[67] Especially for studies on high-elevation sites, the use of more accurate sensors and ventilation systems should be considered. High-quality data sets in these environments are very rare, but can provide more detailed insights on the relevance of the processes discussed in the paper [*Marty et al.*, 2002].

## Appendix A

[68] In the following, we report the values of the RMSE between modeled and observed longwave radiation for all-sky conditions at both the calibration site T1 (Table A1) and at the four validation sites (Table A2) for the whole period of record.

[69] **Acknowledgments.** The authors would like to thank Ben Brock for providing the Miage station data, Edoardo Cremonese and Umberto Morra di Cella for the data of Cime Bianche and Tsa de Tsan, and Marco Carenzo for the T2 data. Five anonymous reviewers provided very useful comments that considerably improved the manuscript, and are gratefully acknowledged.

## References


Abramowitz, G., L. Pouyanné, and H. Ajami (2012), On the information content of surface meteorology for downward atmospheric long-wave radiation synthesis, *Geophys. Res. Lett.*, *39*, L04,808, doi: 10.1029/2011GL050726.

Alados-Arboledas, L. (1993), Estimation of hourly values of downward atmospheric radiation under cloudless skies during day- and night-time conditions, *Theor. Appl. Climatol.*, *48*, 127–131, doi: 10.1007/BF00864919.

Alados-Arboledas, L., J. Vida, and F. J. Olmo (1995), The estimation of thermal atmospheric radiation under cloudy conditions, *Int. J. Climatol.*, *15*, 107–116, doi:10.1002/joc.3370150513.

Allen, R., L. Pereira, D. Raes, and M. Smith, (1998), Crop evapotranspiration-guidelines for computing crop water requirements, *FAO Irrigation and Drainage Paper 56*, Food and Agriculture Organization of the United Nations.

Ångström, A. (1916), Über die Gegenstrahlung der Atmosphäre, *Meteorol. Z.*, *33*, 529–538.

Anslow, F. S., S. Hostetler, W. R. Bidlake, and P. U. Clark (2008), Distributed energy balance modelling of South Cascade Glacier, Washington and assessment of model uncertainty, *J. Geophys. Res.*, *113*(F02019), doi: 10.1029/2007JF000850.

Arnold, N. S., I. C. Willis, M. J. Sharp, K. S. Richards, and W. J. Lawson (1996), A distributed surface energy-balance model for a small valley glacier. I. Development and testing for Haut Glacier d'Arolla, Valais, Switzerland, *J. Glaciol.*, *42*(140), 77–89.

Bolz, H. M. (1949), Die Abhängigkeit der infraroten Gegenstrahlung von der Bewölkung, *Z. Meteorol.*, *7*, 201–203.

Brock, B. W., and N. S. Arnold (2000), A spreadsheet-based (Microsoft Excel) point surface energy balance model for glacier and snowmelt studies, *Earth Surf. Processes Landforms*, *25*, 649–658, doi: 10.1002/1096-9837(200006)25:6<649::AID-ESP97>3.0.CO;2-U.

Brock, B. W., I. C. Willis, and M. J. Sharp (2000a), Measurement and parameterization of albedo variations at Haut Glacier d'Arolla, Switzerland, *J. Glaciol.*, *46*(155), 675–688, doi:10.3189/172756500781832675.

Brock, B. W., I. C. Willis, M. J. Sharp, and N. S. Arnold (2000b), Modelling seasonal and spatial variations in the surface energy balance of Haut Glacier d'Arolla, Switzerland, *Ann. Glaciol.*, *31*, 53–62, doi: 10.3189/172756400781820183.

Brock, B. W., C. Mihalcea, M. P. Kirkbride, G. Diolaiuti, M. E. J. Cutler, and C. Smiraglia (2010), Meteorology and surface energy fluxes in the 2005–2007 ablation seasons at the Miage debris-covered glacier, Mont Blanc Massif, Italian Alps, *J. Geophys. Res.*, *115*(D9), D09,106, doi: 10.1029/2009JD013224.

Brunt, D. (1932), Notes on radiation in the atmosphere, *Quat. J. R. Meteorol. Soc.*, *58*, 389–420, doi:10.1002/qj.49705824704.

Brutsaert, W. (1975), On a derivable formula for long-wave radiation from clear skies, *Water Resour. Res.*, *11*(5), 742–744, doi:10.1029/WR011i005p00742.

Campbell (2009), *CNR1 Net Radiometer, Instruction Manual*, Campbell Scientific Ltd., Logan, Utah.

Carenzo, M., F. Pellicciotti, S. Rimkus, and P. Burlando (2009), Assessing the transferability and robustness of an enhanced–emperature index glacier melt model, *J. Glaciol.*, *55*(190), 258–274, doi:10.3189/002214309788608804.

Chedin, A., N. A. Scott, C. Wahiche, and P. Moulinier (1985), The improved initialization inversion method: A high resolution physical method for temperature retrievals from satellites of the TIROS-N series, *J. Clim. Appl. Meteorol.*, *24*(2), 128–143, doi:10.1175/1520-0450(1985)024<0128:TIIIMA>2.0.CO;2.

Corripio, J. (2003), Vectorial algebra algorithms for calculating terrain parameters from DEMs and solar radiation modelling in mountainous terrain, *Int. J. Geogr. Inf. Sci.*, *17*(1), 1–23, doi:10.1080/713811744.

Crawford, T. M., and C. E. Duchon (1999), An improved parameterization for estimating effective atmospheric emissivity for use in calculating daytime downwelling longwave radiation, *J. Appl. Meteorol.*, *38*, 474–480, doi:10.1175/1520–0450(1999)038<0474:AIPFEE>2.0.CO;2.

Cremonese, E., U. M. di Cella, and F. Pellicciotti, (2007), Dinamica di fusione nivo-glaciale del Ghiacciaio di Tsa de Tsan in Valpelline e stima dell'equivalente in acqua del manto nevoso in bacini di interesse per la produzione idroelettrica in Valle d'Aosta, *Tech. Rep.*, Agenzia Regionale per la Protezione dell'Ambiente della Valle d'Aosta.

Cutler, P., and D. S. Munro (1996), Visible and near-infrared reflectivity during the ablation period on Peyto Glacier, Alberta, Canada, *J. Glaciol.*, *42*(141), 333–340.

Dadic, R., J. Corripio, and P. Burlando (2008), Mass-balance estimates for Haut Glacier d'Arolla, Switzerland, from 2000 to 2006 using DEMs and distributed mass-balance, *Ann. Glaciol.*, *49*, 22–26, doi: 10.3189/172756408787814816.

Deacon, E. L. (1970), The derivation of swinbank's long-wave radiation formula, *Quat. J. R. Meteorol. Soc.*, *96*(408), 313–319, doi: 10.1002/qj.49709640814.

Dilley, A. C., and D. M. O'Brien (1998), Estimating downward clear sky long-wave irradiance at the surface from screen temperature and precipitable water, *Quat. J. R. Meteorol. Soc.*, *124*, 1391–1401, doi: 10.1002/qj.49712454903.

Finch, J. W., and M. J. Best (2004), The accuracy of downward short- and long-wave radiation at the Earth's surface calculated using simple models, *Meteorol. Appl.*, *11*, 33–39, doi:10.1017/S1350482703001154.

Flerchinger, G. N., W. Xaio, D. Marks, T. J. Sauer, and Q. Yu (2009), Comparison of algorithms for incoming atmospheric long-wave radiation, *Water Resour. Res.*, *45*(W03423), doi:10.1029/2008WR007394.

Greuell, W., and R. Böhm (1998), 2m temperatures along melting mid-latitude glaciers, and implications for the sensitivity of the mass balance to variations in temperature, *J. Glaciol.*, *44*(146), 9–20.

Greuell, W., and P. Smeets (2001), Variations with elevation in the surface energy balance on the Pasterze (Austria), *J. Geophys. Res.*, *106*(D23), 31,717–31,727, doi:10.1029/2001JD900127.

Greuell, W., W. H. Knap, and P. C. Smeets (1997), Elevational changes in meteorological variables along a midlatitude glacier during summer, *J. Geophys. Res.*, *102*(D22), 25,941–25,954, doi:10.1029/97JD02083.

Gröbner, J., S. Wacker, L. Vuilleumier, and N. Kämpfer (2009), Effective atmospheric boundary layer temperature from longwave radiation measurements, *J. Geophys. Res.*, *114*, doi:10.1029/2009JD012274.

Gubler, S., S. Gruber, and R. S. Purves (2012), Uncertainties of parameterized surface downward clear-sky shortwave and all-sky longwave radiation, *Atmos. Chem. Phys.*, *12*(11), 5077–5098, doi:10.5194/acp-12-5077-2012.

Gupta, S. K. (1989), A parameterization for longwave surface radiation from sun-synchronous satellite data, *J. Climate*, *2*(4), 305–320, doi: 10.1175/1520-0442(1989)002<0305:APFLSR>2.0.CO;2.

Gupta, S. K., W. L. Darnell, and A. C. Wilber (1992), A parameterization for longwave surface radiation from satellite data: Recent improvements, *J. Appl. Meteorol.*, *31*(12), 1361–1367, doi:10.1175/1520-0450(1992)031<1361:APFLSR>2.0.CO;2.

Halldin, S., and A. Lindroth (1992), Errors in net radiometry—Comparison and evaluation of six radiometer designs, *J. Atmos. Oceanic Technol.*, *9*(6), 762–783, doi:10.1175/1520-0426(1992)009<0762:EINRCA>2.0.CO;2.

Hatfield, J. L., R. J. Reginato, and S. B. Idso (1983), Comparison of longwave radiation calculation methods over the United States, *Water Resour. Res.*, *19*, 285–288, doi:10.1029/WR019i001p00285.

Idso, S. B. (1981), A set of equations for full spectrum and 8- to 14 $\mu$m and 10.5- to 12.5 $\mu$m thermal radiation from cloudless skies, *Water Resour. Res.*, *17*, 295–304, doi:10.1029/WR017i002p00295.

Idso, S. B., and R. D. Jackson (1969), Thermal radiation from the atmosphere, *J. Geophys. Res.*, *74*, 5397–5403, doi:10.1029/JC074i023p05397.

Iqbal, M. (1983), *An Introduction to Solar Radiation*, Academic Press, London.

Iziomon, M. G., H. Mayer, and A. Matzarakis (2003), Downward atmospheric longwave irradiance under clear and cloudy skies: Measurement and parameterization, *J. Atmos. Sol.–Terr. Phys.*, *65*, 1107–1116, doi: 10.1016/j.jastp.2003.07.007.

Kasten, F., and G. Czeplak (1980), Solar and terrestrial radiation dependent on the amount and type of cloud, *Sol. Energy*, *24*, 177–189, doi: 10.1016/0038–092X(80)90391–6.

Kimball, B. A., S. B. Idso, and J. K. Aase (1982), A model of thermal radiation from partly cloudy and overcast skies, *Water Resour. Res.*, *18*, 931–936, doi:10.1029/WR018i004p00931.

König-Langlo, G., and E. Augstein (1994), Parameterization of the downward long-wave radiation at the Earth's surface in polar regions, *Meteorol. Z.*, *3*, 343–347.

Konzelmann, T., R. S. W. van de Wal, W. Greuell, R. Bintanja, E. A. C. Henneken, and A. Abe-Ouchi (1994), Parameterization of global and longwave incoming radiation for the Greenland ice sheet, *Global Planet. Change*, *9*, 143–164, doi:10.1016/0921-8181(94)90013-2.

Kuipers Munneke, P., C. H. Reijmer, and M. R. van den Broeke (2011), Assessing the retrieval of cloud properties from radiation measurements over snow and ice, *Int. J. Climatol.*, *31*(5), 756–769, doi:10.1002/joc.2114.

Laevastu, T. (1960), *Factors affecting the temperature of the surface layer of the sea*.

Lhomme, J., J. Vacher, and A. Rocheteau (2007), Estimating downward long-wave radiation on the Andean Altiplano, *Agric. For. Meteorol.*, *145*, 139–148, doi:10.1016/j.agrformet.2007.04.007.

MacDonell, S., L. Nicholson, and C. Kinnard (2013), Parameterisation of incoming longwave radiation over glacier surfaces in the semiarid Andes

of Chile, *Theor. Appl. Climatol., Online first*, *111*(3–4), 513–528, doi: 10.1007/s00704-012-0675-1.

Marthews, T., Y. Malhi, and H. Iwata (2012), Calculating downward longwave radiation under clear and cloudy conditions over a tropical lowland forest site: An evaluation of model schemes for hourly data, *Theor. Appl. Climatol.*, *107*, 461–477, doi:10.1007/s00704-011-0486-9.

Marty, C., and R. Philipona (2000), The clear-sky index to separate clear-sky from cloudy-sky situations in climate research, *Geophys. Res. Lett.*, *27*(17), 2649–2652, doi:10.1029/2000GL011743.

Marty, C., R. Philipona, C. Frohlich, and A. Ohmura (2002), Altitude dependence of surface radiation fluxes and cloud forcing in the Alps: Results from the alpine surface radiation budget network, *Theor. Appl. Climatol.*, *72*(3-4), 137–155, doi:10.1007/s007040200019.

Maykut, G. A., and P. E. Church (1973), Radiation climate of Barrow Alaska, 1962–66, *J. Appl. Meteorol.*, *12*, 620–628, doi:10.1175/1520–0450(1973)012<0620:RCOBA>2.0.CO;2.

Michel, D., R. Philipona, C. Ruckstuhl, R. Vogt, and L. Vuilleumier (2008), Performance and uncertainty of CNR1 net radiometers during a one-year field comparison, *J. Atmos. Oceanic Technol.*, *25*, 442–451, doi: 10.1175/2007JTECHA973.1.

Mölg, T., N. J. Cullen, and G. Kaser (2009), Solar radiation, cloudiness and longwave radiation over low-latitude glaciers: Implications for mass-balace modelling, *J. Glaciol.*, *55*(190), 292–302, doi: 10.3189/002214309788608822.

Munro, D. S., and G. J. Young (1982), An operational net shortwave radiation model for glacier basins, *Water Resour. Res.*, *18*(2), 220–230, doi: 10.1029/WR018i002p00220.

Niemelä, S., P. Räisänen, and H. Savijärvi (2001), Comparison of surface radiative flux parameterisations. Part I: Longwave radiation, *Atmos. Res.*, *58*, 1–18, doi:10.1016/S0169-8095(01)00084-9.

Ohmura, A. (1981), *Climate and Energy Balance on Arctic Tundra, Zürcher Geographische Schriften*, vol. 3, Geographical Institute of the Swiss Federal Institute of Technology, Zürich.

Ohmura, A. (2001), Physical basis for the temperature-based melt-index method, *J. Appl. Meteorol.*, *40*, 753–761, doi:10.1175/1520-0450(2001)040<0753:PBFTTB>2.0.CO;2.

Pellicciotti, F., J. Helbing, A. Rivera, V. Favier, J. Corripio, J. Araos, J. E. Sicart, and M. Carenzo (2008), A study of the energy balance and melt regime on Juncal Norte Glacier, semi-arid Andes of central Chile, using melt models of different complexity, *Hydrol. Processes*, *22*, 3980–3997, doi:10.1002/hyp.7085.

Pellicciotti, F., M. Carenzo, J. Helbing, S. Rimkus, and P. Burlando (2009), On the role of the subsurface heat conduction in glacier energy balance modelling, *Ann. Glaciol.*, *50*, 16–24, doi:10.3189/172756409787769555.

Pellicciotti, F., T. Raschle, T. Huerlimann, M. Carenzo, and P. Burlando (2011), Transmission of solar radiation through clouds on melting glaciers: A comparison of parameterisations and their impact on melt modelling, *J. Glaciol.*, *57*(202), 367–381, doi: 10.3189/002214311796406013.

Petersen, L., F. Pellicciotti, I. Juszak, M. Carenzo, and B. W. Brock (2013), Suitability of a constant air temperature lapse rate over an Alpine glacier: Testing the Greuell and Böhm model as an alternative, *Ann. Glaciol.*, *54*(63), 1–1, doi:10.3189/2013AoG63A477.

Plüss, C., and A. Ohmura (1997), Longwave radiation on snow-covered mountainous surfaces, *J. Appl. Meteorol.*, *36*(6), 818–824, doi: 10.1175/1520-0450(1997)036<0818:LROSCM>2.0.CO;2.

Prata, A. J. (1996), A new, long-wave formula for estimating downward clear-sky radiation at the surface, *Quat. J. R. Meteorol. Soc.*, *122*, 1127–1151, doi:10.1002/qj.49712253306.

Ruckstuhl, C., and R. Philipona (2008), Detection of cloud-free skies based on sunshine duration and on the variation of global solar irradiance, *Meteorol. Z.*, *17*(2), 181–186, doi:10.1127/0941-2948/2008/0271.

Satterlund, D. R. (1979), An improved equation for estimating long-wave radiation from the atmosphere, *Water Resour. Res.*, *15*, 1649–1650, doi: 10.1029/WR015i006p01649.

Schade, N. H., A. Macke, H. Sandmann, and C. Stick (2009), Total and partial cloud amount detection during summer 2005 at Westerland (Sylt, Germany), *Atmos. Chem. Phys.*, *9*(4), 1143–1150, doi:10.5194/acp-9-1143-2009.

Sedlar, J., and R. Hock (2009), Testing longwave radiation parameterizations under clear and overcast skies at Storglaciären, Sweden, *The Cryosphere*, *3*, 75–84.

Sicart, J. E., J. W. Pomeroy, R. L. H. Essery, and D. Bewley (2006), Incoming longwave radiation to melting snow: Observations, sensitivity and estimation in northern environments, *Hydrol. Processes*, *20*, 3697–3708, doi:10.1002/hyp.6383.

Sicart, J. E., R. Hock, P. Ribstein, and J. P. Chazarin (2010), Sky longwave radiation on tropical Andean glaciers: Parameterization and sensitivity to atmospheric variables, *J. Glaciol.*, *56*, 854–860, doi: 10.3189/002214310794457182.

Stenning, A. J., C. E. Banfield, and G. J. Young (1981), Synoptic controls over katabatic layer characteristics above a melting glacier, *J. Climatol.*, *1*(4), 309–324, doi:10.1002/joc.3370010404.

Strasser, U., J. Corripio, F. Pellicciotti, P. Burlando, B. Brock, and M. Funk (2004), Spatial and temporal variability of meteorological variables at Haut Glacier d'Arolla, Switzerland, during the ablation season 2001: Measurements and simulations, *J. Geophys. Res.*, *109*(D3), doi: 10.1029/2003JD003973.

Sugita, M., and W. Brutsaert (1993), Cloud effect in the estimation of instantaneous downward longwave radiation, *Water Resour. Res.*, *29*, 599–605, doi:10.1029/92WR02352.

Swinbank, W. C. (1963), Long-wave radiation from clear skies, *Quat. J. R. Meteorol. Soc.*, *89*, 339–348, doi:10.1002/qj.49708938105.

Swinbank, W. C. (1964), Long-wave radiation from clear skies, *Quat. J. R. Meteorol. Soc.*, *90*(386), 488–493, discussion, doi:10.1002/qj.49709038617.

Unsworth, M. H., and J. L. Monteith (1975), Long-wave radiation at the ground 1. Angular distribution of incoming radiation, *Quat. J. R. Meteorol. Soc.*, *105*, 13–24, doi:10.1002/qj.49710142703.

van As, D., M. van den Broeke, C. Reijmer, and R. van de Wal (2005), The summer surface energy balance of the high Antarctic plateau, *Boundary-Layer Meteorol.*, *115*(2), 289–317, doi:10.1007/s10546-004-4631-1.

van den Broeke, M., D. van As, C. Reijmer, and R. van de Wal (2004), Assessing and improving the quality of unattended radiation observations in Antarctica, *J. Atmos. Oceanic Technol.*, *21*(9), 1417–1431, doi: 10.1175/1520-0426(2004)021<1417:AAITQO>2.0.CO;2.